

Uncovering Redox Non-Innocent H-Bonding in Cu(I)-Diazene Complexes

Evan J. Gardner,[†] Sean C. Marguet,[‡] Caitlyn R. Cobb,[†] Dominic M. Pham,[†] Jeffery A. Bertke,[†] Hannah S. Shafaat,^{*,‡} and Timothy H. Warren^{*,†}

[†]Department of Chemistry, Georgetown University, Box 51277-1227, Washington, D.C. 20057, United States

[‡]The Ohio State University, 100 West 18th Avenue, Columbus, Ohio 43210, United States

KEYWORDS Hydrogen-bonding, Copper, Diazene, Redox Non-Innocence

ABSTRACT: The life-sustaining reduction of N₂ to NH₃ is thermoneutral yet kinetically challenged by high energy intermediates such as N₂H₂. Exploring intramolecular H-bonding as a potential strategy to stabilize diazene intermediates, we employ a series of [X^{Het}TpCu]₂(μ-N₂H₂) complexes that exhibit H-bonding between pendant aromatic N-heterocycles (X^{Het}) such as pyridine and a bridging *trans*-N₂H₂ ligand at copper(I) centers. X-ray crystallography and IR spectroscopy clearly reveal H-bonding in [py^{Me}TpCu]₂(μ-N₂H₂) while low temperature ¹H NMR studies coupled with DFT analysis reveals a dynamic equilibrium between two closely related, symmetric H-bonded structural motifs. Importantly, the X^{Het} pendant negligibly influences the electronic structure of X^{Het}TpCu^I centers in X^{Het}TpCu(CNAr^{2,6-Me2}) complexes that lack H-bonding as judged by nearly indistinguishable ν(CN) frequencies (2113 - 2117 cm⁻¹). Nonetheless, H-bonding in the corresponding [X^{Het}TpCu]₂(μ-N₂H₂) complexes results in marked changes in ν(NN) (1398 - 1419 cm⁻¹) revealed through rRaman studies. Due to the closely matched N-H BDE's of N₂H₂ and the neutral pyH⁰ cation radical, the aromatic N-heterocyclic pendants may encourage partial H-atom transfer (HAT) from N₂H₂ to X^{Het} through redox non-innocent H-bonding in [X^{Het}TpCu]₂(μ-N₂H₂). DFT studies reveal modest thermodynamic barriers for concerted transfer of both H-atoms of coordinated N₂H₂ to the X^{Het} pendants to generate tautomeric [X^{HetH}TpCu]₂(μ-N₂) complexes, identifying concerted dual HAT as a thermodynamically favorable pathway for N₂ / N₂H₂ interconversion.

The nearly 200 MT/yr industrial production of ammonia (NH₃) via the Haber-Bosch process provides a lifeline of bio-available nitrogen required to sustain life.^{1,2} Owing to the large volumes of H₂ consumed by this process, contemporary NH₃ production ultimately relies on H₂ feedstocks like fossil CH₄ and coal.²⁻⁴ Consequently, NH₃ production, which inherits its sizable carbon footprint from H₂ synthesis, emits 1-2% of the world's CO₂.⁵ Additionally, the centralization of industrial NH₃ synthesis around H₂ feedstocks contributes to geopolitical disparities in affordable fertilizer access.⁶ Nascent efforts to utilize NH₃ as a carbon-free energy vector similarly reckon with the unsustainability of NH₃ mass production.^{1,7} Yet, NH₃ oxidation methods such as H₂ cracking⁸ or electrocatalytic oxidation⁹⁻¹² may be key in availing strategies to tackle the microscopic reverse: sustainable N₂ reduction to NH₃. The nearly thermoneutral N₂ reduction and NH₃ oxidation suggests proton-coupled electron transfer (PCET) as an attractive approach to minimize kinetic barriers between intermediates.

N₂ / NH₃ interconversion involves a nexus of high energy nitrogenous intermediates that involve N-H bond forming and bond breaking reactions. When performed in 2 e⁻ / 2 H⁺ steps, high-energy intermediates such as diazene (N₂H₂) and hydrazine (N₂H₄) pose thermodynamic challenges to the overall this interconversion (Figure 1).¹³ Efficient N₂ reduction¹⁴⁻¹⁷ and NH₃ oxidation,¹⁸⁻²¹ therefore, each share the need to lower

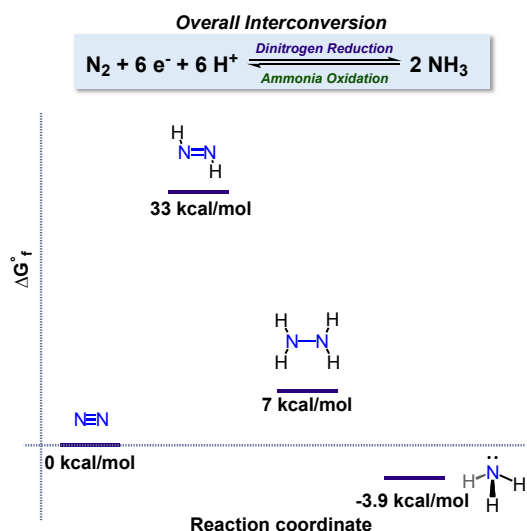


Figure 1. Free energy coordinate diagram for 2 e⁻ / 2 H⁺ steps in N₂ ↔ NH₃ interconversion. Free energies of formation for N₂H₂ and N₂H₄ based on calculated thermochemical data.¹³

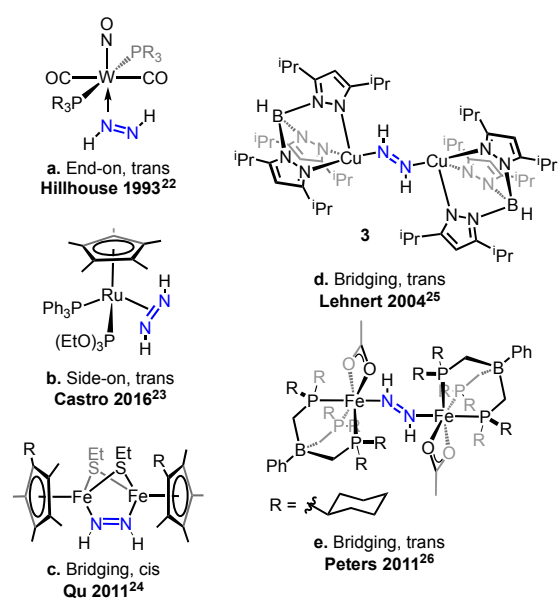


Figure 2. Complexes exhibiting various metal-diazene coordination modes.

barriers through high-energy intermediates such as N_2H_2 and N_2H_4 when proceeding via $2 H^+ / 2 e^-$ steps.

Here, N_2H_2 reigns as the highest energy intermediate, uphill in free energy from both N_2 (+33 kcal/mol) and N_2H_4 (+26 kcal/mol) (Figure 1).¹³ Therefore, stabilization of N_2H_2 intermediates in N_2 / NH_3 interconversion systems can thermodynamically level the species involved for the efficient interconversion of near-thermoneutral N_2 and NH_3 . Known transition metal diazene complexes reveal a range of N_2H_2 coordination motifs (Figure 2).^{22–27} Since the lifetime of free diazene is so short in solution (aqueous N_2H_2 decay: $k = 2.2 \times 10^4 M^{-1}s^{-1}$ at 25 °C),²⁸ isolable metal-diazene complexes enable the study of N_2H_2 and the effects of coordination at metal centers by a wider variety of spectroscopic and other direct methods.^{22–54}

Recent exploration of dynamic secondary coordination sphere Lewis acid and H-bonding interactions include metal-

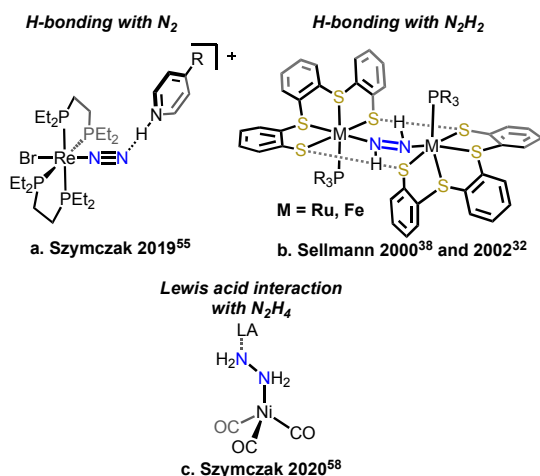


Figure 3. Secondary coordination sphere H-bonding with N_2 , N_2H_2 , and N_2H_4 ligands.

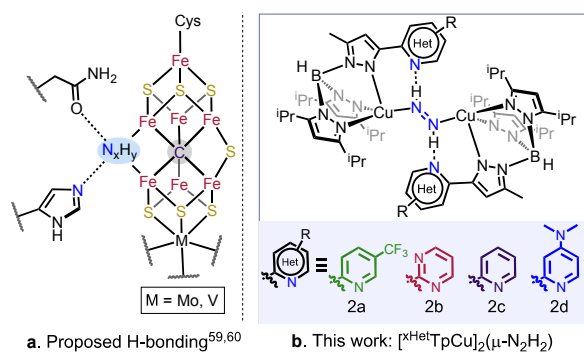


Figure 4. (a) Suggested H-bonding to reduced nitrogenous intermediates at Fe cluster in nitrogenases.^{59,60} (b) This work: H-bonding between aromatic N-donor heterocycles and *trans*- N_2H_2 .

N_2 (Figure 3a)^{55–57} and metal- N_2H_4 (Figure 3c)⁵⁸ complexes that accent studies by Sellmann and coworkers which outline secondary coordination sphere H-bonding with N_2H_2 ligands (Figure 3b).^{31–42} Guided by a developing understanding of the nitrogenase FeMo-cofactor, Sellmann’s complexes modelled possible cluster sulfur- N_2H_2 H-bonding interactions.⁴⁵ These complexes, typically hosting Ru or Fe centers, possess “bifurcated” H-bonding whereby the N_2H_2 ligand simultaneously engages in a short and long H-bonding interaction with proximal S-donors (Figure 3b). More recent structural evidence for FeV- and FeMo-cofactors, however, suggests reduced nitrogenous intermediates may engage in more dynamic H-bonding with proximal N-donor residues (Figure 4a).^{59,60} Considering N_2H_2 as a critical, high-energy intermediate in N_2 reduction, we seek to illuminate the effects of H-bonding between aromatic N-heterocycles with coordinated N_2H_2 (Figure 4b).

We previously reported a series of $[^{xHet}TpCu]_2(\mu-OH)_2$ complexes **1** that offer tunable secondary coordination sphere H-bonding interactions via pendant aromatic heterocyclic N-donor arms (Figure 5).⁶¹ Employing this family of $[^{xHet}TpCu]_2(\mu-OH)_2$ species, we set out to synthesize and characterize the corresponding $[^{xHet}TpCu]_2(\mu-N_2H_2)$ complexes **2a** – **2d** to examine the effect of H-bonding against the closely related $[^{iPr_2}TpCu]_2(\mu-N_2H_2)$ (**3**) species²⁵ that lacks H-bonding (Figure 2d).

Although Cu(I) may appear to be an unusual metal center to examine coordinated N_2H_2 , limited d - π^* backbonding from

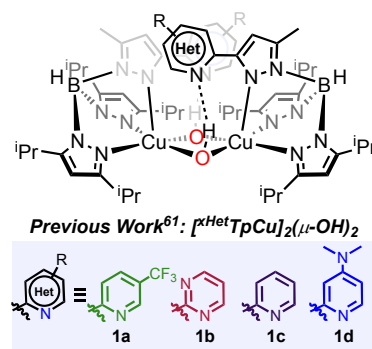


Figure 5. A series of complexes $[^{xHet}TpCu]_2(\mu-OH)_2$ (**1**) possessing pendant heterocycles for tunable second sphere H-bonding interactions.

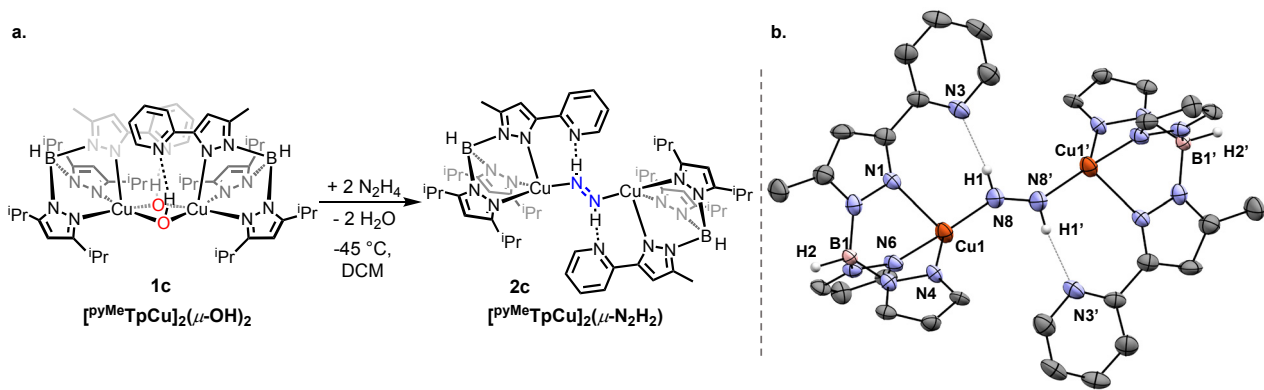


Figure 6. (a) Synthesis of $[\text{pyMeTpCu}]_2(\mu\text{-N}_2\text{H}_2)$ (**2c**) from $[\text{pyMeTpCu}]_2(\mu\text{-OH})_2$ (**1c**). (b) X-ray structure of $[\text{pyMeTpCu}]_2(\mu\text{-N}_2\text{H}_2)$ (**2c**) (isopropyl groups and most H-atoms omitted for clarity).

low energy Cu d-orbitals as well as the reluctance of d^{10} Cu(I) centers to undergo reduction by N_2H_4 enables affords the opportunity to examine the effect of H-bonding involving diazene N-H bonds on the N=N interaction. Additionally, diamagnetic Cu(I) complexes enable the study of dynamic intramolecular H-bonding via NMR spectroscopic techniques. Since diazene possesses weak N-H bonds (N-H BDFE = 27 kcal/mol),^{13,62} there is the possibility of H-atom transfer (HAT) to the intramolecular aromatic N-heterocycle (^xHet) involved in H-bonding in the targeted $[\text{X}^{\text{Het}}\text{TpCu}]_2(\mu\text{-N}_2\text{H}_2)$ complexes: the pyridinium radical pyH^0 has a similar N-H BDFE (35 kcal/mol).^{2,63} Thus, ^xHet H-bonding to N_2H_2 may involve redox non-innocence that stems from the possibility of HAT. Reported herein is the first systematic study that probes the impact of intramolecular H-bonding with N_2H_2 using ligands featuring tunable pendant H-bond acceptors.

Results and Discussion

Synthesis of $[\text{pyMeTpCu}]_2(\mu\text{-N}_2\text{H}_2)$ (**2c**)

The synthesis of the dicopper(I) diazene complex $[\text{pyMeTpCu}]_2(\mu\text{-N}_2\text{H}_2)$ (**2c**) mirrors the synthesis of $[\text{iPr}_2\text{TpCu}]_2(\mu\text{-N}_2\text{H}_2)$ (**3**) prepared upon addition of hydrazine to $[\text{iPr}_2\text{TpCu}]_2(\mu\text{-OH})_2$.⁶⁴ Addition of N_2H_4 to a dichloromethane solution of blue $[\text{pyMeTpCu}]_2(\mu\text{-OH})_2$ (**1c**) at low temperature leads to a gradual color change to maroon $[\text{pyMeTpCu}]_2(\mu\text{-N}_2\text{H}_2)$ (**2c**) over 4 h (Figure 6a). Subsequent crystallization of **2c** from a supersaturated dichloromethane solution at -45 °C for 14 h yielded X-ray quality platelet crystals in 74% isolated yield.

The single crystal X-ray structure of $[\text{pyMeTpCu}]_2(\mu\text{-N}_2\text{H}_2)$ (**2c**) reveals symmetrical H-bonding between the pendant pyridine and diazene N-H bonds, resulting in a crystallographic inversion center through the diazene N-N bond that relates the two Cu centers (Figure 6b). The diazene N8-N8' distance of 1.248(10) Å and Cu1-N8 distance of 1.892(5) Å are closely related to the diazene N=N and Cu-N distances in an independently prepared sample of $[\text{iPr}_2\text{TpCu}]_2(\mu\text{-N}_2\text{H}_2)$ (**3**) (N7-N7' 1.239(7), Cu1-N7 1.918(3) Å) that does not possess intramolecular H-bonding (Figure S19). Further distortion of the tetrahedral copper coordination environment of **2c** ($\tau_4' = 0.67$) relative to **3** ($\tau_4' = 0.75$),⁶⁵ may result from the elongation of the pyrazole-copper interaction (N1-Cu: 2.271(5) Å) in **2c** to accommodate *py*-diazene H-bonding.

In $[\text{pyMeTpCu}]_2(\mu\text{-N}_2\text{H}_2)$ (**2c**) the N atoms of the pendant pyridyl (N3) and bridging diazene (N8) are clearly within H-bonding range (N3-(H)N8: 2.08 (8) Å). Allowing the diazene H-atom to refine after placement in an idealized position results in a nearly linear N3 \cdots H-N8 vector with an angle of 168(8)°. These metrical parameters within the H-bonding interactions are consistent with those reported in Fe(II) and Ru(II) diazene complexes (N \cdots H: 2.201 – 3.858 Å) which possess bifurcated H-bonding between thiolate donors and a bridging *trans*-diazene (Figure 3b).^{36,42}

NMR Characterization of $[\text{pyMeTpCu}]_2(\mu\text{-N}_2\text{H}_2)$ (**2c**)

The low temperature ^1H NMR spectrum of **2c** in dichloromethane- d_2 at -50 °C reveals a broad downfield resonance at 15.7 ppm (Figure 7a). We assign this signal as the diazene *HN=NH* resonance ($\delta_{\text{N-H}}$) which appears in the range 12 – 18 ppm in other diamagnetic diazene complexes.^{26,36} Prepared from copper(II) hydroxide **1c** and $^{15}\text{N}_2\text{H}_4$, the ^1H NMR spectrum of the ^{15}N isotopologue $[\text{pyMeTpCu}]_2(\mu\text{-}^{15}\text{N}_2\text{H}_2)$ (**2c**^{15N}) exhibits a distinct doublet at $\delta_{\text{N-H}}$ at 15.7 ppm with $^1J_{\text{N-H}} = 64$ Hz at -60 °C (Figure 7a). At even lower temperature (-80 °C), the ^1H NMR spectrum of C_{2h} -symmetric **2c**^{15N} reveals an AA'XX' system due to coupling between magnetically inequivalent ^1H and ^{15}N nuclei. NMR lineshape simulation of this AA'XX' system provides coupling constants $^1J_{\text{NH}} = -64$ Hz, $^2J_{\text{NH}} = 1$ Hz, $^1J_{\text{NN}} = 10$ Hz and $^3J_{\text{HH}} = 23$ Hz (Figure S11). The vicinal $^3J_{\text{HH}}$ coupling is within the range of reported in previously characterized diazene complexes ($^3J_{\text{HH}} = 21 - 30$ Hz).^{26,27,31} Moreover, other diamagnetic C_{2h} -symmetric ^{15}N -labeled diazene complexes such as $[(\text{B}_2\text{Pz}_4\text{Py})\text{Fe}](\mu\text{-N}_2\text{H}_2)$ ²⁷ and $[\text{PhBP}^{\text{CH}_2\text{Cy}}_3]\text{Fe}(\text{OAc})_2(\mu\text{-N}_2\text{H}_2)$ ²⁶ also exhibit characteristic AA'XX' in ^1H NMR spectra.

Curiously, in our characterization of the known **3**^{15N} isotopomer in dichloromethane- d_2 at -50 °C, we observed a downfield peak at 12.4 ppm that possesses an AA'XX'-like splitting pattern (Figure S8). While attempts to fully model the AA'XX' pattern of this weak signal were unsuccessful, we observe strong $^1J_{\text{NH}}$ (-54 Hz) coupling characteristic of a N_2H_2 ligand. The nearly 3.3 ppm downfield shift of $\delta_{\text{N-H}}$ for **2c**^{15N} in comparison to **3**^{15N} reflects deshielding of the $\delta_{\text{N-H}}$ resonances via intramolecular H-bonding in **2c**^{15N}.

Unexpectedly, ^1H NMR spectra of **2c** contain an additional minor downfield peak at 13.8 ppm that is also sensitive to ^{15}N -diazene isotopic substitution (Figure 7). The lineshape simula-

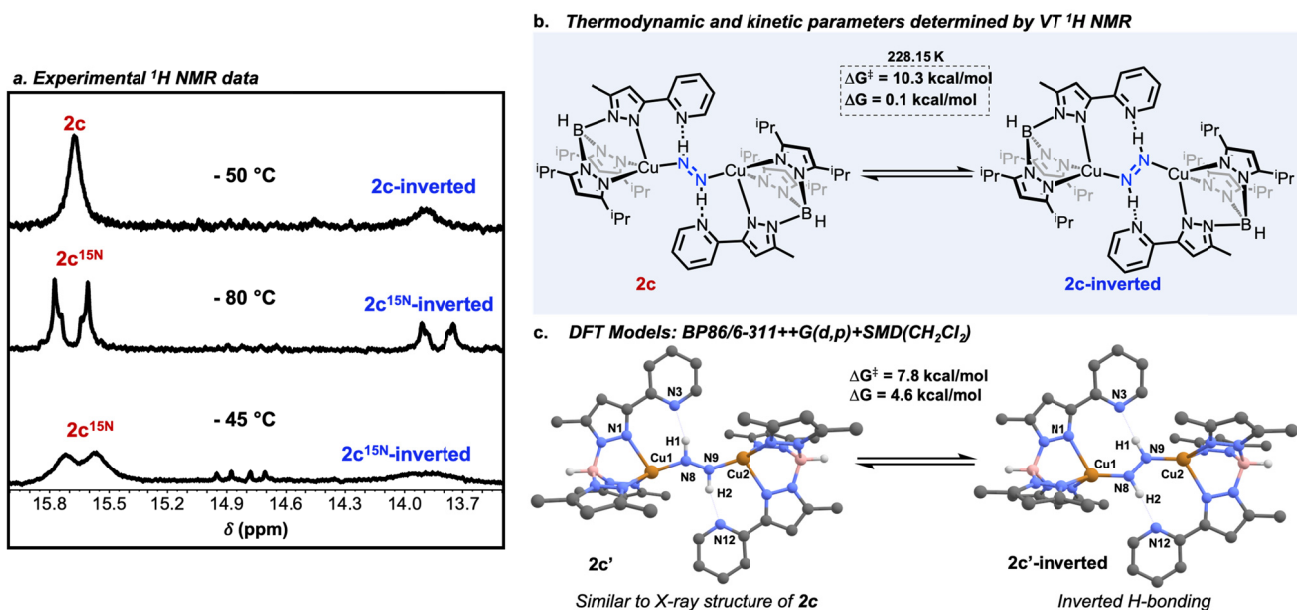


Figure 7. (a) Stacked ^1H NMR spectra (400 MHz in dichloromethane- d_2) comparing **2c** at $-50\text{ }^\circ\text{C}$ with **2c** $^{15\text{N}}$ at $-80\text{ }^\circ\text{C}$ and $-45\text{ }^\circ\text{C}$. (b) Proposed interconversion of H-bonding modes between **2c** (left) and **2c-inverted** (right) with kinetic and thermodynamic parameters determined by variable temperature ^1H NMR experiments. (c) DFT (BP86/6-311++g(d,p)+SMD(CH₂Cl₂)) optimized structures of **2c'** (left) and **2c'-inverted** (right) with calculated $\Delta G(298\text{K})$ for the **2c'** to **2c'-inverted** transformation. For computational efficiency, **2c'** and **2c'-inverted** models possess Me substituents in place of $i\text{Pr}$ groups found in experimental compounds **2c**.

tion of the AA'XX' pattern provides approximate coupling constants $^1J_{\text{NH}} = -65\text{ Hz}$, $^2J_{\text{NH}} = 2\text{ Hz}$, $^1J_{\text{NN}} = 5\text{ Hz}$ and $^3J_{\text{HH}} = 27\text{ Hz}$ which are also consistent with a diazene ligand. We assign this additional resonance observed in NMR spectra of **2c** to the isomer **2c-inverted** that features H-bonding between a pendant py arm and the distal N-H bond of the diazene ligand (Figure 7b). This is analogous to Sellmann's Fe and Ru complexes that possess bifurcating H-bonding between N_2H_2 and two proximal S-donors in which they also reported two closely spaced downfield diazene $\delta_{\text{N-H}}$ resonances^{37,40} (15.64 and 15.59 ppm in a $[\text{Fe}(\text{PBU}_3)(\text{tpS}_4)](\mu\text{-N}_2\text{H}_2)$ complex).⁴⁰ At temperatures above $-80\text{ }^\circ\text{C}$, a weak four-line resonance at 14.7 ppm appears ($<10\%$ of total $\delta_{\text{N-H}}$ resonances). This may represent a minor N_2H_2 species forms with even lower symmetry than **2c** $^{15\text{N}}$ and **2c** $^{15\text{N-inverted}}$.

Variable temperature (VT) ^1H NMR spectra reveal dynamic exchange observed between the diazene $\delta_{\text{N-H}}$ resonances of **2c** $^{15\text{N}}$ and **2c** $^{15\text{N-inverted}}$. Distinct at $-80\text{ }^\circ\text{C}$ at 400 MHz, the ^1H NMR $\delta_{\text{N-H}}$ peaks at 15.7 ppm and 13.8 ppm coalesce at $-10\text{ }^\circ\text{C}$. At $-80\text{ }^\circ\text{C}$ these signals appear in a 0.8:0.2 ratio, although the relative intensity of the 13.8 ppm peak slightly increases as the temperature is raised (Figure S12). A van't Hoff analysis between $-80\text{ }^\circ\text{C}$ and $-45\text{ }^\circ\text{C}$ reveals that the interconversion of **2c** $^{15\text{N}}$ to **2c** $^{15\text{N-inverted}}$ is nearly thermoneutral at $-45\text{ }^\circ\text{C}$ ($\Delta G_{228} = 0.1 \pm 0.4\text{ kcal/mol}$, $\Delta H = 3.8 \pm 0.3\text{ kcal/mol}$, $\Delta S = 16.5 \pm 1.4\text{ cal/mol}$). The separation of the two $\delta_{\text{N-H}}$ peaks at temperatures between $-80\text{ }^\circ\text{C}$ and $-30\text{ }^\circ\text{C}$ was used to calculate rate constants for interconversion.⁶⁶ Eyring analysis of interconversion rates between **2c** $^{15\text{N}}$ and **2c** $^{15\text{N-inverted}}$ points to a modest barrier $\Delta G_{228.15}^\ddagger = 10.3 \pm 0.3\text{ kcal/mol}$ (Figure S13).

As both **2c** and **2c-inverted** exhibit $\delta_{\text{N-H}}$ resonances nearly 2 ppm downfield from **3**, this suggests that H-bonding takes place in these complexes bearing the pendant py H-bond acceptor.

Computational Analysis of $[\text{py}^{\text{Me}}\text{TpCu}]_2(\mu\text{-N}_2\text{H}_2)$ Isomers

We employed density functional theory calculations to provide further support for the pair of H-bonded isomers **2c** and **2c-inverted** revealed by ^1H NMR spectra. For computational efficiency, we started from X-ray structural coordinates of **2c**, paring down $i\text{Pr}$ substituents to Me groups in DFT model **2c'** calculated at the BP86/6-311++G(d,p)+SMD(CH₂Cl₂) level of theory. Optimized in the absence of any symmetry constraints, **2c'** is effectively C_1 -symmetric and possesses a similar *trans*- N_2H_2 coordination environment to **2c**, albeit with a somewhat shorter and slightly less linear H-bonding vector ($\text{N}3 \cdots \text{H}1\text{-N}8$ 1.96 Å; $\text{N}3\text{-H}1\text{-N}8$ 159.8°) as well as a shorter Cu-N bond (Cu1-N8 1.88 Å) and longer N=N bond (N8-N9 1.29 Å). The model **2c'-inverted** results from rotating the diazene ligand between copper centers, changing the Cu-N-N-Cu dihedral angle by 180°, followed by optimization. Converged in the absence of symmetry constraints, **2c'-inverted** is effectively C_i -symmetric and gives rise to two symmetric H-bonding vectors with distances and angles ($\text{N}3 \cdots \text{H}1\text{-N}8$ 1.980 Å; $\text{N}3\text{-H}1\text{-N}8$ 167.0°) as well as Cu-N (Cu1-N8 1.876 Å) and N-N (N8-N9 1.290 Å) distances comparable to **2c'** and **2c**. DFT predicts that **2c'-inverted** is higher in energy than **2c'** by 4.6 kcal/mol, in general agreement with thermodynamic data obtained from VT NMR experiments.

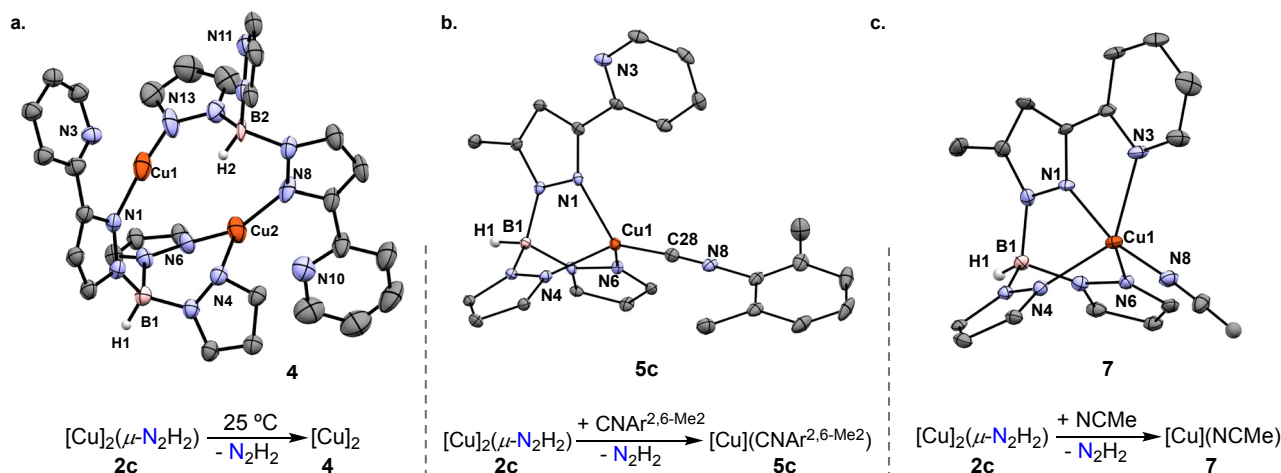
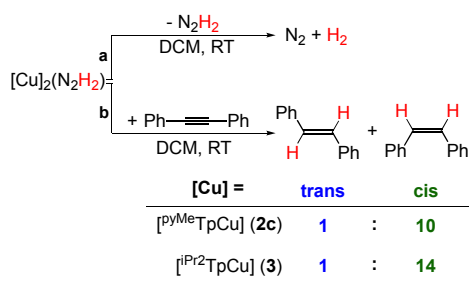


Figure 8. (a) X-ray structure and synthesis of $[\text{py}^{\text{Me}}\text{TpCu}]_2$ with all pyrazole substituents omitted for clarity. (b) X-ray structure and synthesis of $[\text{py}^{\text{Me}}\text{TpCu}(\text{CNAr}^{2,6\text{-Me}_2})]$ (**5c**). (c) X-ray structure and synthesis of $[\text{py}^{\text{Me}}\text{TpCu}(\text{NCMe})]$ (**7**) (isopropyl substituents are omitted for clarity in **4**, **5c**, and **7**).

To estimate the barrier, we computationally explored the species **2c'**-**perpendicular** in which each pendant pyridine arm cannot engage in efficient H-bonding through the constraint of the $\text{N}_{\text{py}}\text{-Cu-N}_{\text{diazene}}\text{-H}$ dihedral angles to 90° (Figure S66). Optimized without symmetry constraints, this orientation prevents efficient $\text{py}\cdots\text{diazene}$ H-bonding. For instance, this model possesses a closest $\text{N}_{\text{py}}\cdots\text{H-N}_{\text{diazene}}$ distance of 3.77 Å and unfavorable, bent $\text{N}_{\text{py}}\cdots\text{H-N}_{\text{diazene}}$ angles of 98.2° . This conformation is uphill in free energy at 298 K from both **2c'** (+7.8 kcal/mol) and **2c'**-**inverted** (+3.2 kcal/mol). The energetic separation roughly corresponds to the barrier $\Delta G_{228,15}^\ddagger = 10.3 \pm 0.3$ kcal/mol observed in the interconversion of **2c** and **2c**-**inverted** experimentally measured by variable temperature VT NMR spectroscopy.

Thermal Loss of N_2H_2 from $[\text{Cu}]_2(\mu\text{-N}_2\text{H}_2)$ Complexes

$[\text{py}^{\text{Me}}\text{TpCu}]_2(\mu\text{-N}_2\text{H}_2)$ (**2c**) exhibits a subtle color change from maroon to light orange in dichloromethane solution at RT over the course of 2 h, whereas $[\text{ipr}^2\text{TpCu}]_2(\mu\text{-N}_2\text{H}_2)$ (**3**) changes from deep purple to light tan over approximately the same timeframe. After stirring at 0°C for 10 min, dichloromethane solutions of **2c** and **3** show detectable amounts of H_2 gas in the headspace as determined by mass spectrometry (Scheme 1; Figure S6). The detection of H_2 is consistent with the decomposition of free N_2H_2 to N_2 and H_2 in solution.^{39,67} Further supporting the loss of free diazene, dichloromethane solutions of **2c** and **3** left to stand at 25°C in the presence of excess diphenylacetylene generate *cis* and *trans* isomers of



Scheme 1. (a) Thermal N_2H_2 -loss and decay to N_2 and H_2 . (b) Thermal N_2H_2 -loss in the presence of diphenylacetylene to give a mixture of *cis*/*trans*-stilbenes.

stilbene (Scheme 1). This represents a method of diazene detection previously employed for $[\text{W}(\text{N}_2\text{H}_2)(\text{CO})_2(\text{NO})(\text{PPh}_3)_2][\text{SO}_3\text{CF}_3]$ that loses diazene in solution.²²

Loss of diazene from $[\text{py}^{\text{Me}}\text{TpCu}]_2(\mu\text{-N}_2\text{H}_2)$ (**2c**) provides a dinuclear $[\text{py}^{\text{Me}}\text{TpCu}]_2$ (**4**) as orange block crystals upon cooling a toluene solution to -40°C after standing at RT for 16 h (Figure 8a). The X-ray structure of **4** reveals a dinuclear coordination preference of the $\text{py}^{\text{Me}}\text{Tp}$ scaffold in the absence of a donor ligand which features a nearly linear, two-coordinate Cu^{I} site (N1-Cu1-N13 $175.4(8)^\circ$) possessing an additional long Cu-py interaction (Cu1-N3 2.371(16) Å) as well as a three-coordinate Cu^{I} site with a Cu-Cu separation of 3.466(2) Å.

In contrast, mononuclear complexes result upon addition of the isonitrile $\text{CNAr}^{2,6\text{-Me}_2}$ ($\text{Ar}^{2,6\text{-Me}_2} = 2,6\text{-Me}_2\text{C}_6\text{H}_3$) or acetonitrile donors to **2c** (Figure 8b,c). The crystal structure of **5c** reveals a four-coordinate Cu(I), distorted tetrahedral ($\tau_4 = 0.7$) center with a Cu1-C28 distance of 1.8305(19) Å. Importantly, the py-donor arm does not coordinate to this copper(I) center. Coordination of the pyridyl pendant to the copper(I) center observed for acetonitrile adduct **7** (Cu1-N3 : 2.328(5) Å) gives rise to a five-coordinate geometry between square pyramidal and trigonal bipyramidal ($\tau_5 = 0.5$).⁶⁸ Moreover, addition of two equiv. $\text{CNAr}^{2,6\text{-Me}_2}$ or NCMe to dinuclear **4** results in rapid conversion to mononuclear **5c** and **7**.

Systematic Study of H-bonding with N_2H_2 by IR Spectroscopy

We employed IR spectroscopy to characterize H-bonding in $[\text{py}^{\text{Me}}\text{TpCu}]_2(\mu\text{-N}_2\text{H}_2)$ (**2c**). A solid sample of **2c** prepared in a KBr pellet exhibits no easily discernable $\nu(\text{NH})$ signals for the diazene ligand near the reported value for $[\text{ipr}^2\text{TpCu}]_2(\mu\text{-N}_2\text{H}_2)$ (**3**) at $\nu(\text{NH}) = 3222\text{ cm}^{-1}$. As it is likely that H-bonding sufficiently red-shifts $\nu(\text{NH})$ into the aromatic and aliphatic $\nu(\text{CH})$ peaks that typically appear in the $3100 - 2750\text{ cm}^{-1}$ region, we prepared the isotopologue $[\text{py}^{\text{Me}}\text{TpCu}]_2(\mu\text{-N}_2\text{D}_2)$ (**2c^D**) from the reaction of copper(II) hydroxide **1c** with $\text{N}_2\text{D}_4\cdot\text{D}_2\text{O}$. The IR spectrum of $[\text{py}^{\text{Me}}\text{TpCu}]_2(\mu\text{-N}_2\text{D}_2)$ (**2c^D**) possesses a broad, yet easily discernable $\nu(\text{ND})$ band at 2236 cm^{-1} from which a Hooke's law estimate for $[\text{py}^{\text{Me}}\text{TpCu}]_2(\mu\text{-N}_2\text{H}_2)$ predicts $\nu(\text{NH})$

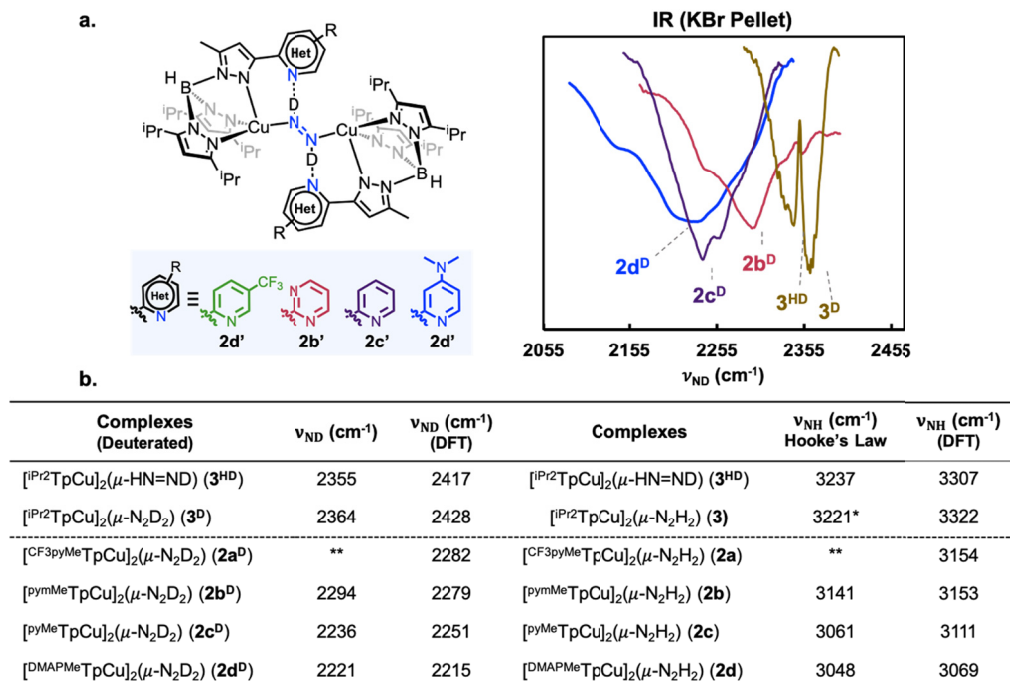


Figure 9. (a) IR spectra of [^{xHet}TpCu]₂(μ -N₂D₂) (**2a^D** – **2d^D**) and [^{iPr}2TpCu]₂(μ -N₂D₂) (**3^D**) taken in KBr pellets. (b) Tabulated $\nu(\text{ND})$ data for complexes **2a^D** – **2d^D** and **3^D** and comparison to Hooke's law estimations of $\nu(\text{NH})$ for corresponding complexes **2a** – **2d** along with DFT calculated frequencies at the BP86/6-311++ G(d,p) level of theory. *Experimentally reported value.²⁵ ** Thermal sensitivity precluded characterization of **2a^D** by IR.

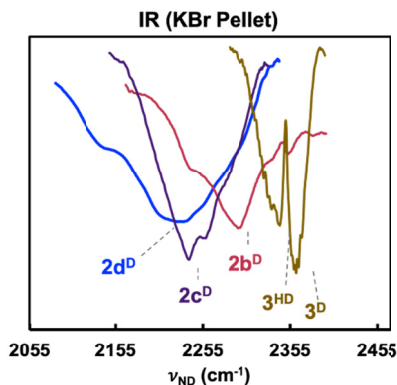
to be centered at 3061 cm⁻¹. Importantly, the broad $\nu(\text{ND})$ stretch for [^{pyMe}TpCu]₂(μ -N₂D₂) is red-shifted nearly 120 cm⁻¹ from the two separate, relatively sharp $\nu(\text{ND})$ stretches observed for [^{iPr}2TpCu]₂(μ -N₂D₂) (**3^D**) (2364 and 2355 cm⁻¹) that does not possess H-bonding.

To modulate the H-bonding interaction between diazene and the pendant aromatic N-heterocycle, we prepared a series of diazene complexes [^{xHet}TpCu]₂(μ -N₂D₂) (**2b^D** – **2d^D**) from the corresponding [^{xHet}TpCu]₂(μ -OH)₂ complexes (**1b** – **1d**).⁶¹ Similar to **2c^D**, we observe broad diazene $\nu(\text{ND})$ bands in the IR spectra of **2b^D** and **2d^D** centered at 2294 cm⁻¹ and 2221 cm⁻¹, respectively, each red shifted relative to **3^D** (2364 cm⁻¹) (Figure 9b). Furthermore, the degree of the $\nu(\text{ND})$ red shift in **2^D** relative to **3^D** tracks directly with the basicity of the pendant aromatic N-heterocycle. This trend is similar to the shift in $\nu(\text{OH})$ observed for [^{xHet}TpCu]₂(μ -OH)₂ (**1a** – **1d**: 3223 – 3340 cm⁻¹) relative to [^{iPr}2TpCu]₂(μ -OH)₂ that lacks H-bonding (3660 cm⁻¹).⁶¹ While the thermal instability of **2a^D** precludes our ability to experimentally determine ν_{ND} under analogous conditions, DFT methods enable predictions of both $\nu(\text{NH})$ and $\nu(\text{ND})$ in isotopologues **2** and **2^D** (Figure 9b).

We attribute the two closely spaced (9 cm⁻¹) (ND) bands in sample **3^D** to a mixture of completely deuterated **3^D** and partially deuterated [^{iPr}2TpCu]₂(μ -HN=ND) (**3^{HD}**), formed from H/D exchange with residual H₂O produced from the reaction of **1c** with N₂D₄•D₂O. DFT models support the close spacing of the (ND) of **3^D** and **3^{HD}** (11 cm⁻¹). While similar H⁺/D⁺ exchange could occur for **2a^D** – **2d^D**, broadening of (ND) bands via H-bonding prevents the identification of multiple distinct peaks.

Assessing the Backbonding Ability of the Copper Center

We sought to assess the pendant aromatic N-heterocycle's effect on the ability of the Cu^I center to engage in π -



backbonding in the absence of any H-bonding interactions. Following preparation by addition of CNAr^{2,6-Me2} to **2a** – **2d** formed *in situ*, we measured the isonitrile C-N stretching frequency $\nu(\text{CN})$ by IR in series of four-coordinate complexes [^{xHet}TpCu(CNAr^{2,6-Me2})] (**5a** – **5d**). Importantly, the aromatic N-heterocycles do not exhibit any interaction with the copper center or its ligands in these tetrahedral isonitrile complexes **5**. The electron density at the Cu^I center available for backbonding is reported in the $\nu(\text{CN})$ stretch of the CNAr^{2,6-Me2} ligand. These $\nu(\text{CN})$ stretches for **5a** – **5d** exhibit a close range between 2113 – 2117 cm⁻¹, similar to [^{iPr}2TpCu(CNAr^{2,6-Me2})] (**6**) at 2109 cm⁻¹ (Figure 10).⁶⁹ These stretches are each only modestly lower from $\nu(\text{CN})$ for free CNAr^{2,6-Me2} (2130 cm⁻¹)⁷⁰ due to modest backbonding from d¹⁰ Cu^I to the isonitrile CN π^* -system. Importantly, the very narrow range of $\nu(\text{CN})$ for **5a** – **5d** and **6** indicate that the aromatic N-heterocycle in **5a** – **5d**

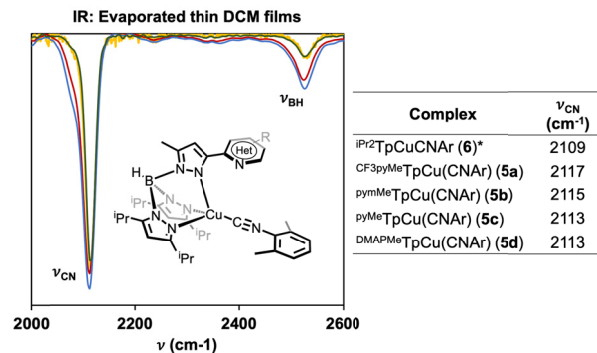


Figure 10. IR spectra of [^{xHet}TpCu(CNAr^{2,6-Me2})] (**5a** – **5d**) taken from evaporated CH₂Cl₂ solutions and tabulation of $\nu(\text{CN})$ stretching frequencies. *Previous reports of [^{iPr}2TpCu(CNAr^{2,6-Me2})] (**6**).⁶⁹

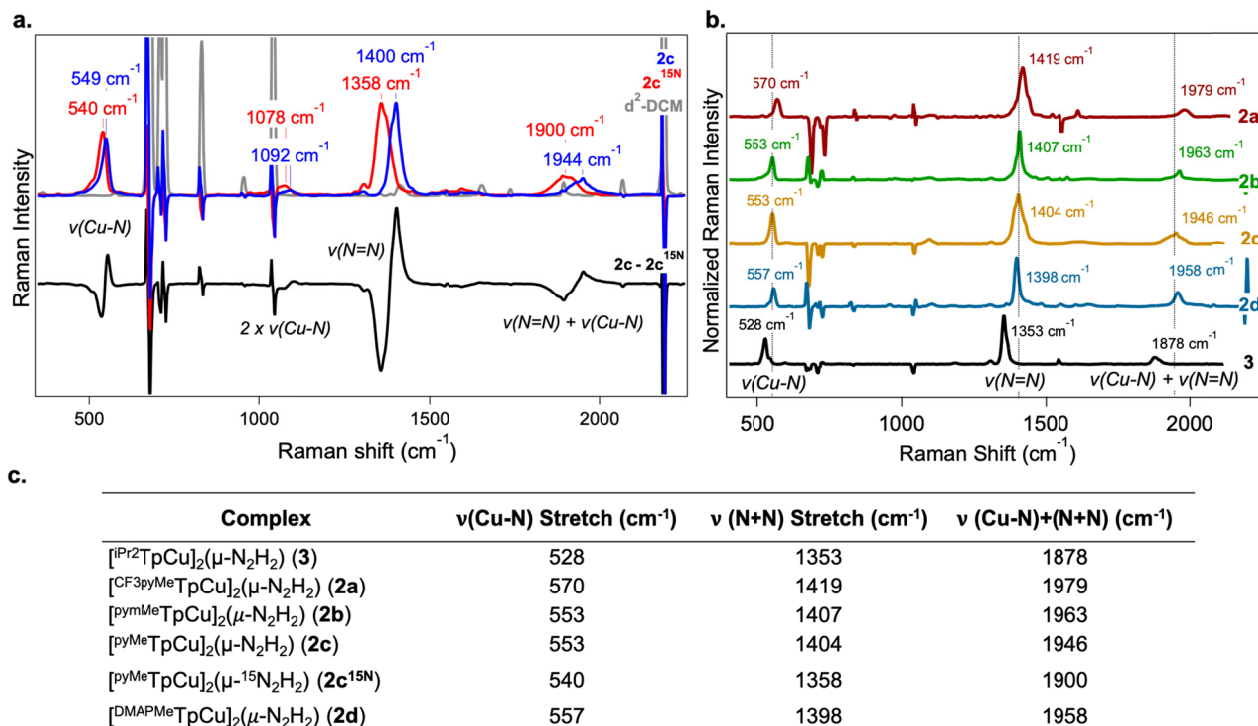


Figure 11. (a) Overlaid rRaman spectra of **2c** and **2c**^{15N} with ¹⁴N-¹⁵N difference spectrum. (b) Comparison of rRaman spectra for **2a** – **2d** and **3**. (c) Tabulated rRaman shifts of interest for **2a** – **2d** and **3**.

only negligibly influences the electronic structure of the Cu^I center in the absence of any H-bonding or coordination interaction with the aromatic N-heterocycle.

DFT vibrational frequency calculations on models **5a'** – **5d'** also predict very minor changes in the electronic structure of the Cu^I center. For instance, the $\nu(\text{CN})$ stretching frequency range of 2082 – 2084 cm^{-1} is narrow and in agreement with experimental findings. Consistent with this observation, **5a'** – **5d'** have very similar HOMO energies (-4.72 to -4.80 eV) as well (Figure S65). These calculations further support that the pendant ^xHet has little influence on the ground state electronic structure of the Cu^I center in the absence of H-bonding.

Resonance Raman Spectroscopy of $[\text{TpCu}]_2(\mu\text{-N}_2\text{H}_2)$ Complexes

Resonance Raman (rR) spectroscopy provides a direct measurement of the degree of activation of the diazene N-N bond, providing insight into the Cu-diazene interaction and its modulation via H-bonding with the pendant N-heterocycle across the series of compounds $[\text{X}^{\text{Het}}\text{TpCu}]_2(\mu\text{-N}_2\text{H}_2)$ (**2a** – **2d**). As the prototypical example, we discuss the resonance Raman spectra of $[\text{pyMeTpCu}]_2(\mu\text{-N}_2\text{H}_2)$ (**2c**) and its isotopomer **2c**^{15N} (Figure 11a). Using 488 nm excitation, the rR spectrum of a frozen dichloromethane solution of **2c** shows an intense band at 1400 cm^{-1} that shifts to 1358 cm^{-1} in **2c**^{15N} ($\Delta\nu_{\text{expt}}(^{14}\text{N}\text{-}^{15}\text{N}) = 42 \text{ cm}^{-1}$). This difference is consistent with a Hooke's law prediction for an approximately local N-N stretching mode ($\Delta\nu_{\text{calc}}(^{14}\text{N}\text{-}^{15}\text{N}) = 47 \text{ cm}^{-1}$) (Figure 11a). We assign an additional prominent band at 549 cm^{-1} ($\Delta\nu(^{14}\text{N}\text{-}^{15}\text{N}) = 9 \text{ cm}^{-1}$) to the Cu-N stretching mode. The observed decrease in energy to 540 cm^{-1} upon ¹⁵N-labelling is less than that expected

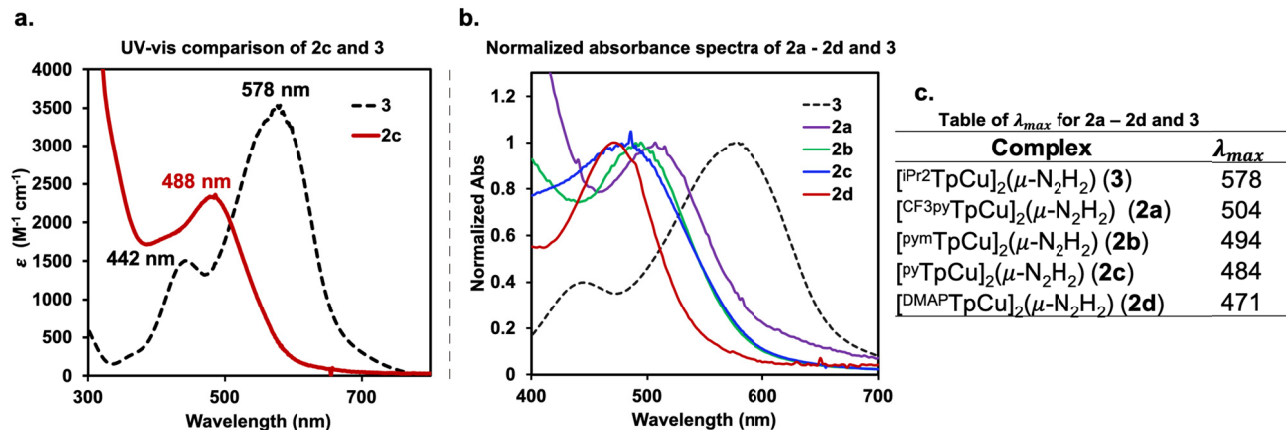
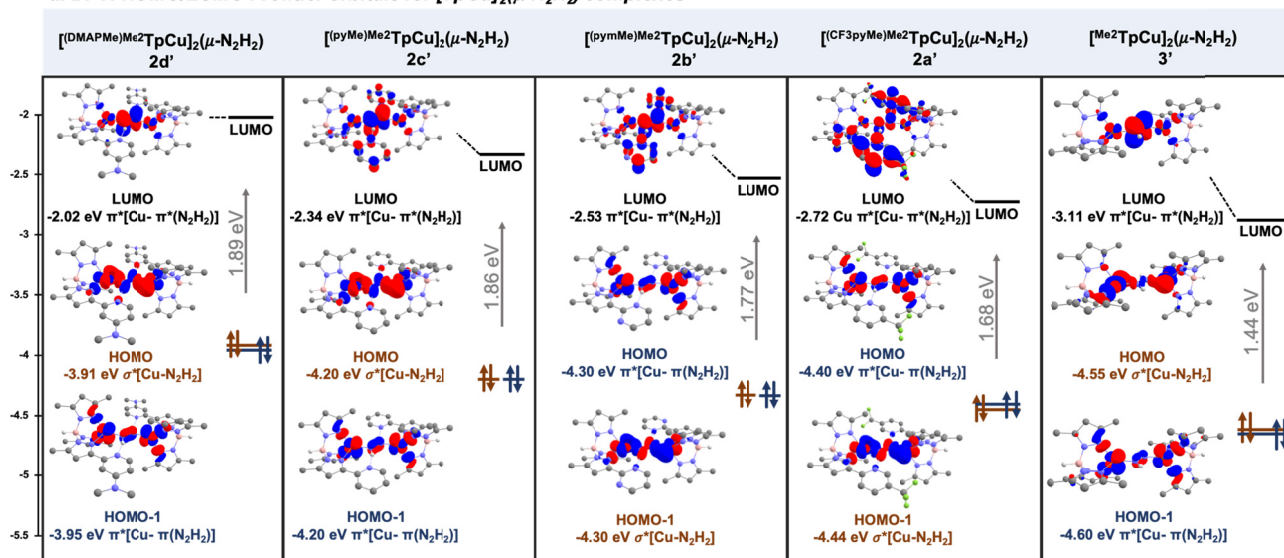


Figure 12. (a) Overlaid UV-vis spectra of $[\text{pyMeTpCu}]_2(\mu\text{-N}_2\text{H}_2)$ (**2c**) and $[\text{iPr}_2\text{TpCu}]_2(\mu\text{-N}_2\text{H}_2)$ (**3**). (b) Overlaid normalized UV-vis spectra of **2a** – **2d** and **3**. (c) Experimental λ_{max} for **2a** – **2d** and **3**. All spectra in CH_2Cl_2 at -45 °C

a. DFT: HOMO/LUMO Frontier orbitals for [TpCu]₂(μ-N₂H₂) complexes



b. DFT: LUMO Composition

Species	LUMO Frontier MO	
	^x Het (%)	N ₂ H ₂ (%)
2a'	29.8	11.0
2b'	12.3	44.1
2c'	7.2	52.5
2d'	1.8	63.7
3'	--	63.5

Figure 13. (a) DFT calculated (BP86/6-311++ G(d,p)+SMD(CH₂Cl₂)) frontier MO energies of the HOMO-1, HOMO, and LUMO levels for models **2a'** – **2d'** (isosurfaces are at 0.03 Å³). (b) Estimated total LUMO contributions by ^xHet and N₂H₂ calculated using Hirshfeld methods.

($\Delta\nu$ (¹⁴N–¹⁵N) = 15 cm⁻¹) for an isolated Cu-N bond, suggesting coupling between the ν (Cu-N_{diazene}) and ν (Cu-N_{pyrazolyl}) modes. Moreover, a pronounced combination ν (N=N) + ν (Cu-N) mode occurs at 1944 cm⁻¹ ($\Delta\nu$ (¹⁴N–¹⁵N) = 44 cm⁻¹) along with the overtone of the ν (Cu-N) mode at 1092 cm⁻¹ ($\Delta\nu$ (¹⁴N–¹⁵N) = 14 cm⁻¹). Few other bands appear, indicative of a localized MLCT excitation, consistent with the predicted charge difference density (CDD) from TD-DFT calculations (Figures S80 – S84).

Comparison between the rR spectra of pyridyl-substituted [^{pyMe}TpCu]₂(μ-N₂H₂) (**2c**) and [^{iPr2}TpCu]₂(μ-N₂H₂) (**3**) reveal many common features with similar resonance enhancement patterns. Both compounds exhibit a low degree of anharmonicity for the N-N and Cu-N modes, as evidenced by overtone and combination frequencies that are almost exactly sums of the energies of the parent bands. Highly harmonic overtones are typical for strong, localized bonds. Nonetheless, there are important differences between the two compounds. The ν (N=N) and ν (Cu-N) modes occur at substantially higher energies for **2c** (1404 and 553 cm⁻¹) relative to **3** (1353 and 528 cm⁻¹), although both are significantly lower than free *trans*-N₂H₂ (1529 cm⁻¹).⁷¹ Moreover, the band at 1547 cm⁻¹ of **3** attributed to the N-N-H bending mode is absent in **2c**. This low-intensity mode should occur at lower frequencies upon H-bonding to the pendant pyridine and may shift to such an extent to mix with the N=N mode as previously described for Fe(II)-diazene compounds.⁴³ Additionally, the N-N-H bending mode could be suppressed due to the high intensity of the stretching modes. Vibrational frequency calculations suggest

that the N-N-H bending mode of **2c** would occur at 1502 cm⁻¹, with $\Delta\nu$ (¹⁴N–¹⁵N) = 9 cm⁻¹.

The increase in ν (N=N) and ν (Cu-N) energies for **2c** relative to **3** is clearly linked to H-bonding between N₂H₂ and the pyridyl pendants. In the absence of any H-bonding interactions, the ^{pyMe}TpCu and ^{iPr2}TpCu fragments possess nearly identical backbonding ability as judged by the IR spectra of the corresponding pyramidal ^{xHet}TpCu(CNAr^{2,6-Me2}) (**5c**) and ^{iPr2}TpCu(CNAr^{2,6-Me2}) (**6**) complexes (Figure 10).

Resonance Raman spectra of **2a** – **2d**, which feature increasingly basic N-heterocycle arms across the series, reveal a clear trend from the electronic structure changes (Figure 11): The less basic the N-heterocycle pendant H-bond acceptor, the higher ν (N=N) observed. For instance, **2d**, with the most electron-rich H-bond acceptor, exhibits ν (N=N) of 1398 cm⁻¹ while the ν (N=N) of **2a**, with the least basic (most electron withdrawing) H-bond acceptor, is observed at 1419 cm⁻¹. We also note that the highest value of ν (Cu-N) (570 cm⁻¹) occurs in **2a** while the ν (Cu-N) frequencies of the other derivatives **2b** – **2d** span a narrow range (553 – 557 cm⁻¹).

Electronic Structure of [^{xHet}TpCu]₂(μ-N₂H₂) Complexes

Optical absorption spectra measured in dichloromethane at -45 °C reveal a clear difference between the electronic structures of [^{xHet}TpCu]₂(μ-N₂H₂) (**2a** – **2d**) and [^{iPr2}TpCu]₂(μ-N₂H₂) (**3**) attributable to the pendant aromatic N-heterocycle in **2a** – **2d** (Figure 12). While compound **3** exhibits a strong visible absorption band at 578 nm, **2a** exhibits an optical band with a maximum absorbance at 504 nm (Figure 12). This peak

maximum becomes further blueshifted as the N-heterocyclic arm becomes more basic, with the optical maximum for **2d** at 471 nm (Figure 12).

DFT molecular orbital analyses uncover critical electronic differences that result from the intramolecular H-bonding to diazene. A previous report assigns the strong visible band of **3** at $\lambda_{\max} = 578$ nm ($\epsilon = 3500$ M⁻¹ cm⁻¹) to the HOMO/LUMO charge transfer transition.²⁵ Our DFT calculations on the geometry-optimized model of **3**, denoted **3'**, assign the HOMO as a $\sigma^*[\text{Cu-N}_2\text{H}_2]$ interaction while the LUMO has $\pi^*[\text{Cu-}\pi^*(\text{N}_2\text{H}_2)]$ character (Figure 13). In comparison, **2a'** - **2d'** possess a nearly degenerate set of $\sigma^*[\text{Cu-N}_2\text{H}_2]$ and $\pi^*[\text{Cu-}\pi^*(\text{N}_2\text{H}_2)]$ orbitals while the LUMO level is comprised of $\pi^*[\text{Cu-}\pi^*(\text{N}_2\text{H}_2)]$ orbitals with mixtures of the $\pi^*(\text{N}_2\text{H}_2)$ and $\pi^*(\text{N-heterocycle})$ molecular orbitals (Figure 13). The H-bonding interactions present in **2a'** - **2d'** lead to HOMO levels that increase in energy as the N-heterocycle becomes more basic (-4.40 to -3.91 eV), each higher in energy than the HOMO of **3'** (-4.55 eV) that lacks H-bonding (Figure 13). This direct effect on the HOMO level by the pendant aromatic N-heterocycle requires electronic engagement via H-bonding. For instance, the HOMO levels are essentially constant (-4.72 to -4.80 eV) in the series of isocyanide complexes $[\text{X}^{\text{Het}}\text{TpCu}(\text{CNR}^{2,6-\text{Me}_2})]$ (**5a'** - **5d'**) in which the N-heterocycle pendant does not interact with the copper center or bound isocyanide ligand (Figure S65).

The marked blueshift in λ_{\max} for **2a** - **2d** results from an even more dramatic increase in LUMO energies proportional to the increasing basicity of the N-heterocycle pendant across this series. In models **2a'** - **2d'**, the LUMO increases from -2.72 to -2.02 eV, resulting in an overall increase in the

HOMO/LUMO gap of 1.68 to 1.89 eV. The extent of $\pi^*(\text{N}_2\text{H}_2)$ and $\pi^*(\text{N-heterocycle})$ mixing in the LUMO profoundly depends on the pendant N-heterocycle. The LUMO of most basic DMAP (**2d'**) consists predominantly of $\pi^*(\text{N}_2\text{H}_2)$ character (63.7%), similar to the LUMO of **3'** that lacks H-bonding (63.5%). As the N-heterocycle becomes more electron-poor, an increasing amount of the $\pi^*(\text{N-heterocycle})$ interaction mixes in to give a LUMO for **2a'** that consists of 29.8% $\pi^*(\text{N-heterocycle})$ and only 11.0% $\pi^*(\text{N}_2\text{H}_2)$ (Figure 13b). TD-DFT difference densities also reflect this trend across the series (**2a'** - **2d'**), shifting from an isolated Cu-to-N₂H₂ charge transfer transition (**3a'**) to one with a large degree of density on the N-heterocycle in **2a'** (Figures S80 - S84).

Considering Redox Non-Innocent H-bonding

To integrate the comprehensive structural, spectroscopic, and computational findings of H-bonded diazene compounds $[\text{X}^{\text{Het}}\text{TpCu}]_2(\mu\text{-N}_2\text{H}_2)$ (**2a** - **2d**), we consider a non-canonical role of the pyridine heterocycle. Beyond acting as a proton acceptor, aromatic N-heterocycles such as pyridine can also function as H-atom acceptors upon transfer of both a proton and an electron into the N-heterocycle via H-atom transfer (HAT).⁷² The closely matched average N-H BDFE of N₂H₂ (27 kcal/mol)^{13,62} and calculated N-H BDE of the pyridinium radical pyH^0 (35 kcal/mol)^{2,63} indicates that H-atom transfer from N₂H₂ to the aromatic N-heterocycle pendants along the H-bonding vector in $[\text{X}^{\text{Het}}\text{TpCu}]_2(\mu\text{-N}_2\text{H}_2)$ (**2a** - **2d**) may be thermodynamically possible. Full HAT of both diazene H-atoms from N₂H₂ to the pendant aromatic N-heterocycles in **2a** - **2d** represents a redox tautomerization that generates dicop-

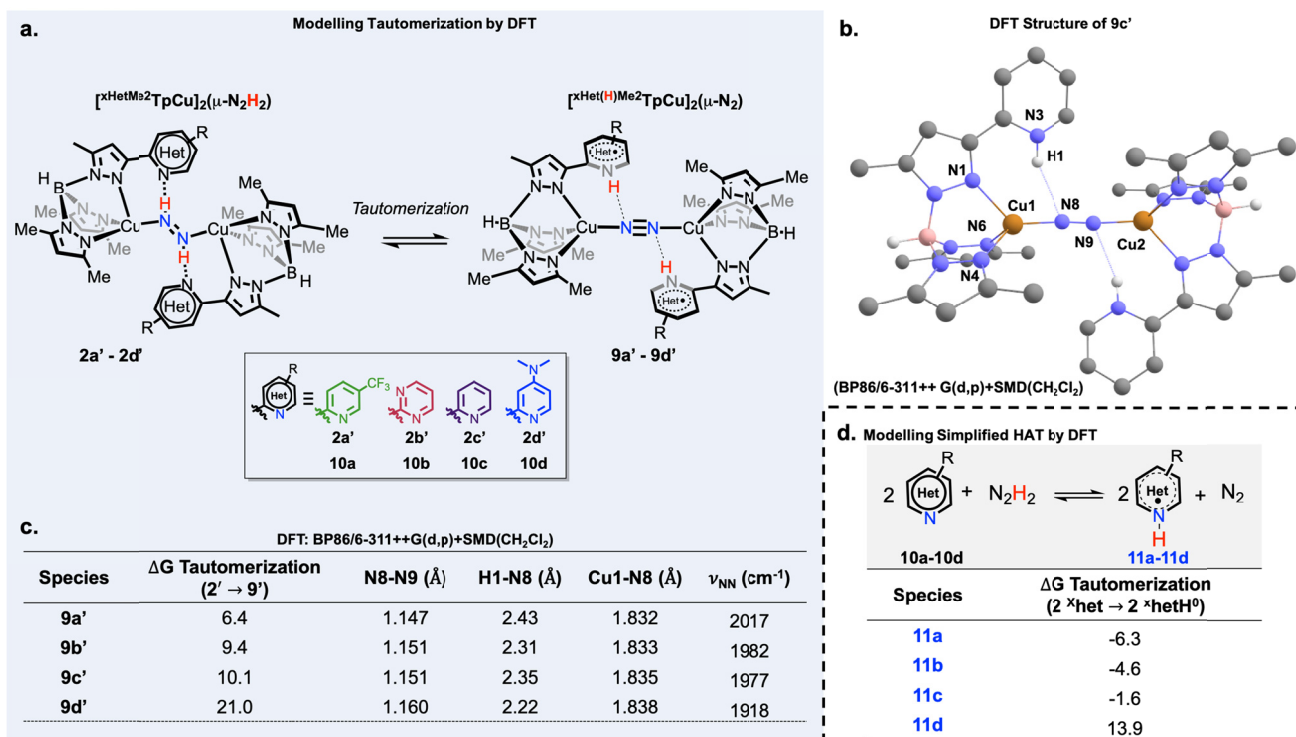


Figure 14. (a) Proposed tautomerization upon concerted transfer of hydrogen atoms from N₂H₂ to H-bonding ^XHet pendants. (b) DFT model of **9c'** at the BP86/6-311++ G(d,p) level of theory with select H-atoms rendered. (c) DFT optimized tautomer complexes **9a'** - **9d'** modeled at the BP86/6-311++ G(d,p)+SMD(CH₂Cl₂) level of theory. (d) DFT modelling of double HAT between N₂H₂ and free aromatic N-heterocycles ^XHet (**10a** - **10d**) to form N₂ and ^XHetH⁰.

per dinitrogen complexes $[\text{}^{\text{xHetH}}\text{TpCu}]_2(\mu\text{-N}_2)$ (**9a** – **9d**). In each case, the aromatic N-heterocycles become pyridinium-type radicals pyH^0 (Figure 14a). We note that the related dicopper dinitrogen complex $[\text{}^{\text{iPr}_2}\text{TpCu}]_2(\mu\text{-N}_2)$ has been structurally and spectroscopically characterized with an N-N distance of 1.111(6) Å and $\nu(\text{NN}) = 2130 \text{ cm}^{-1}$ pointing to a gently reduced N_2 ligand.⁷³

We modeled these redox tautomers **9a'** – **9d'** by DFT as triplet species because in the prototypical case of **9c'** (Figure 14b), the triplet configuration is 7 kcal/mol more stable than the unrestricted open-shell singlet **9c'-singlet** (Table S3). Although these pyridinium radical/dinitrogen redox tautomers $[\text{}^{\text{xHetH}}\text{TpCu}]_2(\mu\text{-N}_2)$ (**9a'** – **9d'**) are calculated to be 6.4 – 20.2 kcal/mol higher in free energy at 298 K than the corresponding H-bonded diazene complexes $[\text{}^{\text{xHet}}\text{TpCu}]_2(\mu\text{-N}_2\text{H}_2)$ (**2a'** – **2d'**), there is a clear trend in their relative stabilities (Figure 14c). As the pendant aromatic N-heterocycle becomes more electron deficient, the redox tautomer **9** resulting from dual HAT becomes more thermodynamically accessible. Trends in free energy differences observed between redox tautomers **2'** and **9'** appear in calculated free energies for dual HAT from free N_2H_2 to a pair of free aromatic N-heterocycles (Figure 14d). Free energies for dual HAT range from -6.3 kcal/mol for the most electron-poor heterocycle (**10a**) to +13.9 kcal/mol for the most electron-rich heterocycle (**10d**; DMAP). Indeed, the resonance Raman spectra of **2a** – **2d** support the contribution of partial redox tautomerization to the electronic structure. All of the H-bonded N_2H_2 ligands show an upshifted $\nu(\text{N}=\text{N})$ frequency relative to that in **3**, indicative of increased $\text{N}=\text{N}$ multiple bonding character. Moreover, the frequency increases as the heterocycle becomes more electron-deficient, consistent with greater contribution of the redox tautomer's greater contribution as HAT becomes more favorable.

The resulting N_2 ligand in redox tautomers **9** also becomes modified through interaction with the N-H moiety of the pyridinium-type radicals $\text{}^{\text{xHetH}}$ that can serve as H-atom donors. In $[\text{}^{\text{xHetH}}\text{TpCu}]_2(\mu\text{-N}_2)$ models **9a'** – **9d'**, the N-N bond and $\text{}^{\text{xHet}}(\text{N})\cdots\text{H}$ bond distances increase with increasing electron richness of the pendant aromatic N-heterocycle. Tautomer **9a'** with the most electron-poor N-heterocycle possesses an only mildly reduced N_2 ligand ($d(\text{N}=\text{N}) = 1.140 \text{ Å}$; $\nu(\text{NN}) = 2060 \text{ cm}^{-1}$) with metric and spectroscopic parameters for the bound N_2 ligand quite similar to those experimentally determined for $[\text{}^{\text{iPr}_2}\text{TpCu}]_2(\mu\text{-N}_2)$.⁷³ On the other hand, electronic communication between the pendant N(H)-heterocycle radicals and the N_2 ligand is clearly evident in DMAP based **9d'** that possesses the most potent H-atom donor. This results in a significantly more reduced N_2 ligand ($d(\text{N}=\text{N}) = 1.151 \text{ Å}$; $\nu(\text{NN}) = 1924 \text{ cm}^{-1}$). The $\text{N}_{\text{Het}}\text{-H}\cdots\text{N}_2\cdots\text{H-N}_{\text{Het}}$ interaction also results in a transfer of spin density from the pyridinium-type radical to the N_2 ligand that increases in these triplet species from **9a'** (8%) to **9d'** (32%) as the strength of the intramolecular H-atom donor increases. While we acknowledge the potential limitations of DFT in the computational analysis of redox tautomers $[\text{}^{\text{xHetH}}\text{TpCu}]_2(\mu\text{-N}_2)$ (**9a'** – **9d'**) relative to the respective ground state structures $[\text{}^{\text{xHet}}\text{TpCu}]_2(\mu\text{-N}_2\text{H}_2)$ (**2a'** – **2d'**), the size and complexity of these models render more sophisticated, multi-configurational calculation methods beyond the reach of this study. Nonetheless, the thermodynamic matching of diazene and pyridinium radical N-H bond strengths clearly supports the thermodynamic possibility of dual HAT along the H-

bonding vectors in the experimentally characterized diazene complexes $[\text{}^{\text{xHet}}\text{TpCu}]_2(\mu\text{-N}_2\text{H}_2)$ (**2a** – **2d**).

Conclusions

We report a unique family of $[\text{}^{\text{xHet}}\text{TpCu}]_2(\mu\text{-N}_2\text{H}_2)$ (**2a** – **2d**) complexes that feature tunable intramolecular H-bonding between modular $\text{}^{\text{xHet}}$ pendants and N_2H_2 . Unambiguously revealed by X-ray crystallography and IR spectroscopy of $[\text{}^{\text{py}}\text{TpCu}]_2(\mu\text{-N}_2\text{H}_2)$ (**2c**), variable temperature ^1H NMR studies indicate that the pendant aromatic N-heterocycles provide a dynamic H-bonding environment to the bridging *trans*- N_2H_2 ligand. This H-bonding introduces profound changes in electronic structure mediated through the $\text{}^{\text{xHet}}\text{N}\cdots\text{HN}=\text{NH}\cdots\text{NHet}^{\text{x}}$ linkage.

Interaction along this linkage leads to a marked increase in $\nu(\text{NN})$ in $[\text{}^{\text{xHet}}\text{TpCu}]_2(\mu\text{-N}_2\text{H}_2)$ complexes (1398 – 1419 cm^{-1}) relative to electronically similar $[\text{}^{\text{iPr}_2}\text{TpCu}]_2(\mu\text{-N}_2\text{H}_2)$ with $\nu(\text{NN})$ at 1353 cm^{-1} . This is an especially significant difference since the related isonitrile complexes $\text{}^{\text{xHet}}\text{TpCu}(\text{CNAr}^{2,6\text{-Me}_2})$ and $\text{}^{\text{iPr}_2}\text{TpCu}(\text{CNAr}^{2,6\text{-Me}_2})$ exhibit nearly indistinguishable isonitrile stretching frequencies $\nu(\text{CN})$ of 2113–2117 and 2109 cm^{-1} , respectively. These closely spaced stretching frequencies indicate that the d^{10} copper(I) fragments $\text{}^{\text{xHet}}\text{TpCu}^{\text{I}}$ and $\text{}^{\text{iPr}_2}\text{TpCu}^{\text{I}}$ possess nearly identical π -backbonding ability. Nonetheless, H-bonding of the pendant aromatic N-heterocycles $\text{}^{\text{xHet}}$ with diazene turns on an interaction that leads to increased NN bond order, one that is maximized by the most electron-poor, weakest H-bond acceptor.

We rationalize this unusual behavior by considering the *H-atom accepting* ability of these pendant aromatic N-heterocycles which increases as they become more electron-poor. Dual, symmetric transfer of H-atoms from weak diazene N-H bonds (average N-H BDFE = 27 kcal/mol) to the aromatic N-heterocycle is thermodynamically matched as the pyH^0 N-H bond is only marginally stronger (BDFE = 35 kcal/mol). Accordingly, dual HAT from the diazene ligand along the H-bonding pathway to the $\text{}^{\text{xHet}}$ pendants in $[\text{}^{\text{xHet}}\text{TpCu}]_2(\mu\text{-N}_2\text{H}_2)$ (**2a'** – **2d'**) is a redox tautomerization that results in the formation of corresponding $\text{}^{\text{xHetH}}$ radical / dinitrogen complexes $[\text{}^{\text{xHetH}}\text{TpCu}]_2(\mu\text{-N}_2)$ (**9a'** – **9d'**). Indeed, the thermodynamic accessibility of $\text{}^{\text{xHetH}}$ radical / dinitrogen complexes **9** (Figure 14c) scales directly with the H-atom accepting ability of the $\text{}^{\text{xHet}}$ pendant that is favored by electron-withdrawing substituents (Figure 14d).

Since many molecular dinitrogen reduction systems operate with strong reductants and pyridinium-derived acids (pyH^+), transient formation of pyridinium radicals pyH^0 has been considered as a mechanism for stepwise HAT to reactive metal-nitrogen intermediates.^{2,74} For instance, with its reduction potential (-1.77 V vs. Fc^+/Fc)⁷⁵ and pK_a (12.53)⁷⁶ in MeCN, the Bordwell equation calculates a N-H BDFE of 35.8 kcal/mol for pyH^0 .⁷⁷ Many key intermediates in dinitrogen reduction catalytic cycles by discrete metal complexes feature weak N-H bonds such as $[\text{M}]\text{-N}=\text{NH}$ and $[\text{M}]\text{-N}=\text{NH}_2$ calculated at -42.7 and -39.4 kcal/mol, respectively, in the Schrock-type reduction $[\text{Ar}_3\text{N}]\text{Mo}$ system.² We note that protonated metallocenes such as $[\text{Cp}^*\text{Co}(\eta^4\text{-CMe}_5\text{H})]^+$ can also serve as H-atom donors due to their weak C-H bond (BDFE = 29 – 30 kcal/mol).^{63,78}

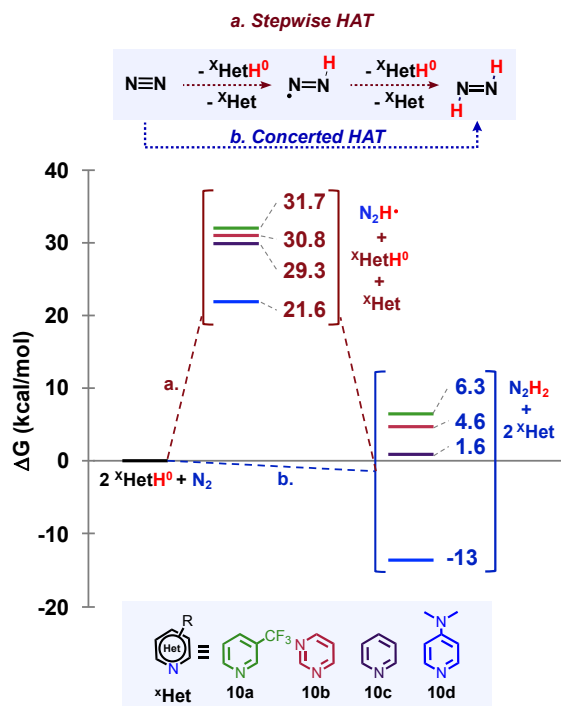


Figure 15. DFT calculated energies for (a) stepwise HAT to N_2 from ${}^x\text{HetH}^0$ vs. (b) concerted HAT to N_2 from $2 {}^x\text{HetH}^0$. Free energies in kcal/mol at 298.15 K.

These observations underscore the significantly lower thermodynamic barriers for simultaneous HAT involving two H-atoms to N_2 to give N_2H_2 as compared to stepwise HAT pathways. For instance, single HAT to free N_2 from pyH^0 must overcome a thermodynamic free energy barrier of 29.3 kcal/mol to give unstable $\text{HN}=\text{N}\cdot$ that can readily accept an additional H-atom from pyH^0 in a subsequent step that is downhill by 27.3 kcal/mol in free energy. If both HAT steps were to occur simultaneously, however, this represents only a modest free energy barrier of +1.6 kcal/mol at this level of theory (Figure 15). While choice of the aromatic N-heterocycle ${}^x\text{Het}$ tunes these energies, stepwise HAT to N_2 intrinsically possesses a higher barrier than simultaneous, dual HAT to N_2 .

The series of compounds $[\text{}^x\text{HetTpCu}]_2(\mu\text{-N}_2\text{H}_2)$ demonstrate that H-bonding modifies diazene in tunable ways within the secondary coordination sphere of well defined, symmetrical metal complexes. Beyond H-bonding, ${}^x\text{Het}$ pendant groups that interact with bound diazene may further modify it through nascent H-atom transfer to these aromatic N-heterocyclic pendants. Symmetric organization of diazene with functionalities that serve both as good *H-bond* and *H-atom* acceptors establishes H-bonding pathways that may be used for H-atom transfer. Performed simultaneously, dual HAT to free N_2 to form N_2H_2 possesses a far lower thermodynamic barrier when carried out in a stepwise fashion. While metal centers undoubtedly stabilize high energy $\text{HN}=\text{N}\cdot$ species via $[\text{M}]\text{-N}=\text{NH}$ intermediates, symmetric metal complex designs that enable dual HAT to $[\text{M}]\text{-N}_2\text{-}[\text{M}]$ intermediates could possess intrinsically lower thermodynamic and kinetic barriers to form $[\text{M}]\text{-N}_2\text{H}_2\text{-}[\text{M}]$ intermediates in N_2 reduction catalysis.

Moreover, metals that only gently reduce N_2 upon binding can facilitate N_2 reduction via H-atom transfer pathways. For

instance, Singh and colleagues have recently reported that electrodeposited Cu films catalyze N_2 reduction to NH_3 in water at $\text{pH} = 13.5$ under ambient conditions with a maximum current density that occurs at an applied potential of -0.5 V vs. RHE.⁷⁹ Thus, discrete copper complexes that outline features relevant to $\text{N}_2 / \text{N}_2\text{H}_2$ interconversion may possess relevance to heterogeneous systems for electrocatalytic ammonia production under mild conditions.¹⁴

Supporting Information

The Supporting Information is available free of charge on the ACS Publications website.

Experimental and X-ray structure details (PDF)

X-ray data for **2c**, **3**, **4**, **5b**, **5c**, **5d**, and **7** (CIF)

AUTHOR INFORMATION

Contributions

Corresponding Author

*E-mail: thw@georgetown.edu

ORCID

Evan J. Gardner: 0000-0003-2945-2951

Sean C. Marguet: 0000-0002-2466-6048

Caitlyn R. Cobb: 0000-0001-5544-0773

Jeffery A. Bertke: 0000-0002-3419-5163

Hannah S. Shafaat: 0000-0003-0793-4650

Timothy H. Warren: 0000-0001-9217-8890

Notes

The authors declare no competing financial interest.

ACKNOWLEDGMENT

THW acknowledges support from the U.S. Department of Energy, Office of Science, Basic Energy Sciences (DE-SC001779). EJG acknowledges support from the ARCS foundation Gladi Mathews fellowship. HSS and SCM acknowledge support from the National Science Foundation (CHE-1454289).

REFERENCES

- (1) Chen, J. G.; Crooks, R. M.; Seefeldt, L. C.; Bren, K. L.; Bullock, R. M.; Darensbourg, M. Y.; Holland, P. L.; Hoffman, B.; Janik, M. J.; Jones, A. K.; et al. Beyond Fossil Fuel-Driven Nitrogen Transformations. *Science* **2018**, *360*, eaar6611.
- (2) Besdek, M. J.; Pappas, I.; Chirik, P. J. Determining and Understanding N-H Bond Strengths in Synthetic Nitrogen Fixation Cycles. In *Topics in Organometallic Chemistry*; Nishibayashi, Y.; Topics in Organometallic Chemistry; Springer International Publishing: Cham, 2017; pp 1–21.
- (3) Razon, L. F. Life Cycle Analysis of an Alternative to the Haber-Bosch Process: Non-Renewable Energy Usage and Global Warming Potential of Liquid Ammonia from Cyanobacteria. *Environ. Prog. Sustain. Energy* **2014**, *33*, 618–624.
- (4) Rafiqul, I.; Weber, C.; Lehmann, B.; Voss, A. Energy Efficiency Improvements in Ammonia Production-Perspectives and Uncertainties. *Energy* **2005**, *30*, 2487–2504.

- (5) Kyriakou, V.; Garagounis, I.; Vourros, A.; Vasileiou, E.; Stoukides, M. *Joule* **2020**, *4*, 142–158.
- (6) Smith, C.; Hill, A. K.; Torrente-Murciano, L. Current and Future Role of Haber–Bosch Ammonia in a Carbon-Free Energy Landscape. *Energy Environ. Sci.* **2020**, *13*, 331–344.
- (7) MacFarlane, D. R.; Cherepanov, P. V.; Choi, J.; Suryanto, B. H. R.; Hodgetts, R. Y.; Bakker, J. M.; Ferrero Vallana, F. M.; Simonov, A. N. A Roadmap to the Ammonia Economy. *Joule* **2020**, *4*, 1186–1205.
- (8) Lee, Y.-J.; Cha, J.; Kwak, Y.; Park, Y.; Jo, Y. S.; Jeong, H.; Sohn, H.; Yoon, C. W.; Kim, Y.; Kim, K.-B.; et al. Top-Down Syntheses of Nickel-Based Structured Catalysts for Hydrogen Production from Ammonia. *ACS Appl. Mater. Interfaces* **2021**, *13*, 597–607.
- (9) Zott, M. D.; Garrido-Barros, P.; Peters, J. C. Electrocatalytic Ammonia Oxidation Mediated by a Polypyridyl Iron Catalyst. *ACS Catal.* **2019**, *9*, 10101–10108.
- (10) Habibzadeh, F.; Miller, S. L.; Hamann, T. W.; Smith, M. R. Homogeneous Electrocatalytic Oxidation of Ammonia to N₂ under Mild Conditions. *Proc. Natl. Acad. Sci.* **2019**, *116*, 2849–2853.
- (11) Raghbi Boroujeni, M.; Greene, C.; Berke, J. A.; Warren, T. H. Chemical and Electrocatalytic Ammonia Oxidation by Ferrocene. *ChemRxiv* **2019**, doi: 10.26434/chemrxiv.9729635.v1.
- (12) Nakajima, K.; Toda, H.; Sakata, K.; Nishibayashi, Y. Author Correction: Ruthenium-Catalysed Oxidative Conversion of Ammonia into Dinitrogen. *Nat. Chem.* **2020**, *12*, 424.
- (13) Matus, M. H.; Arduengo, A. J.; Dixon, D. A. The Heats of Formation of Diazene, Hydrazine, N₂H₃⁺, N₂H₅⁺, N₂H, and N₂H₃ and the Methyl Derivatives CH₃NNH, CH₃NNCH₃, and CH₃HNNHCH₃. *J. Phys. Chem. A* **2006**, *110*, 10116–10121.
- (14) Qing, G.; Ghazfar, R.; Jackowski, S. T.; Habibzadeh, F.; Ashtiani, M. M.; Chen, C.-P.; Smith, M. R.; Hamann, T. W. Recent Advances and Challenges of Electrocatalytic N₂ Reduction to Ammonia. *Chem. Rev.* **2020**, *120*, 5437–5516.
- (15) Roux, Y.; Duboc, C.; Gennari, M. Molecular Catalysts for N₂ Reduction: State of the Art, Mechanism, and Challenges. *ChemPhysChem* **2017**, *18*, 2606–2617.
- (16) Liu, H.; Wei, L.; Liu, F.; Pei, Z.; Shi, J.; Wang, Z.; He, D.; Chen, Y. Homogeneous, Heterogeneous, and Biological Catalysts for Electrochemical N₂ Reduction toward NH₃ under Ambient Conditions. *ACS Catal.* **2019**, *9*, 5245–5267.
- (17) Chalkley, M. J.; Drover, M. W.; Peters, J. C. Catalytic N₂-to-NH₃ (or -N₂H₄) Conversion by Well-Defined Molecular Coordination Complexes. *Chem. Rev.* **2020**, *120*, 5582–5636.
- (18) Dunn, P. L.; Cook, B. J.; Johnson, S. I.; Appel, A. M.; Bullock, R. M. Oxidation of Ammonia with Molecular Complexes. *J. Am. Chem. Soc.* **2020**, *142*, 17845–17858.
- (19) Rees, N. V.; Compton, R. G. Carbon-Free Energy: A Review of Ammonia- and Hydrazine-Based Electrochemical Fuel Cells. *Energy Environ. Sci.* **2011**, *4*, 1255–1260.
- (20) Giddey, S.; Badwal, S. P. S.; Kulkarni, A. Review of Electrochemical Ammonia Production Technologies and Materials. *Int. J. Hydrogen Energy* **2013**, *38*, 14576–14594.
- (21) Valera-Medina, A.; Xiao, H.; Owen-Jones, M.; David, W. I. F.; Bowen, P. J. Ammonia for Power. *Prog. Energy Combust. Sci.* **2018**, *69*, 63–102.
- (22) Smith, M. R.; Cheng, T. Y.; Hillhouse, G. L. Syntheses and Reactions of Hydrazine and Diazene Complexes of Tungsten. The First Example of Monodentate Coordination of Diazene. *J. Am. Chem. Soc.* **1993**, *115*, 8638–8642.
- (23) Albertin, G.; Antoniutti, S.; Botter, A.; Castro, J. Hydrolysis of Coordinated Diazoalkanes To Yield Side-On 1,2-Diazene Derivatives. *Inorg. Chem.* **2015**, *54*, 2091–2093.
- (24) Chen, Y.; Liu, L.; Peng, Y.; Chen, P.; Luo, Y.; Qu, J. Unusual Thiolate-Bridged Diiron Clusters Bearing the Cis-HN=NH Ligand and Their Reactivities with Terminal Alkynes. *J. Am. Chem. Soc.* **2011**, *133*, 1147–1149.
- (25) Fujisawa, K.; Lehnert, N.; Ishikawa, Y.; Okamoto, K. Diazene Complexes of Copper: Synthesis, Spectroscopic Analysis, and Electronic Structure. *Angew. Chem. Int. Ed.* **2004**, *43*, 4944–4947.
- (26) Saouma, C. T.; Moore, C. E.; Rheingold, A. L.; Peters, J. C. A Five-Coordinate Phosphino/Acetate Iron(II) Scaffold That Binds N₂, N₂H₂, N₂H₄, and NH₃ in the Sixth Site. *Inorg. Chem.* **2011**, *50*, 11285–11287.
- (27) Nurdin, L.; Yang, Y.; Neate, P. G. N.; Piers, W. E.; Maron, L.; Neidig, M. L.; Lin, J.-B.; Gelfand, B. S. *Chem. Sci.* **2021**, *12*, 2231–2241.
- (28) Tang, H. R.; Stanbury, D. M. Direct Detection of Aqueous Diazene: Its UV Spectrum and Concerted Dismutation. *Inorg. Chem.* **1994**, *33*, 1388–1391.
- (29) Huttner, G.; Gartzke, W.; Allinger, K. Kristall- Und Molekülstruktur Des Diimin-Komplexes N₂H₂[Cr(CO)₅]₂-2THF. *J. Organomet. Chem.* **1975**, *91*, 47–56.
- (30) Cheng, T.-Y.; Ponce, A.; Hillhouse, G. L.; Rheingold, A. L. Hydroxylamine, Hydrazine, and Diazene as Unidentate Ligands in Osmium and Ruthenium Complexes. *Angew. Chem. Int. Ed.* **1994**, *33*, 657–659.
- (31) Sellmann, D.; Hennige, A. Direct Proof of Trans-Diazene in Solution by Trapping and Isolation of the Trapping Products. *Angew. Chem. Int. Ed.* **1997**, *36*, 276–278.
- (32) Sellmann, D.; Blum, D. C. F.; Heinemann, F. W. Transition Metal Complexes with Sulfur Ligands. Part CLV. Structural and Spectroscopic Characterization of Hydrogen Bridge Diastereomers of [μ-N₂H₂{Fe(PR₃)('tpS₄')}]₂ Diazene Complexes ('tpS₄'²⁻=1,2-bis(2-mercaptophenylthio)phenylene(2-)). *Inorganica Chim. Acta* **2002**, *337*, 1–10.
- (33) Reiher, M.; Salomon, O.; Sellmann, D.; Hess, B. A. Dinuclear Diazene Iron and Ruthenium Complexes as Models for Studying Nitrogenase Activity. *Chem. Eur. J.* **2001**, *7*, 5195–5202.
- (34) Sellmann, D.; Soglowek, W.; Knoch, F.; Moll, M. Nitrogenase Model Compounds: [μ-N₂H₂{Fe('N_HS₄'²⁻)}]₂, the Prototype for the Coordination of Diazene to Iron Sulfur Centers and Its Stabilization through Strong N–H ... S Hydrogen Bonds. *Angew. Chem. Int. Ed.* **1989**, *28*, 1271–1272.
- (35) Wiesler, B. E.; Tuczec, F.; Hennige, A.; Sellmann, D. Activation of Diazene and the Nitrogenase Problem: An Investigation of Diazene-Bridged Fe(II) Centers with Sulfur Ligand Sphere. 2. Vibrational Properties. *J. Am. Chem. Soc.* **1997**, *119*, 8879–8888.
- (36) Sellmann, D.; Friedrich, H.; Knoch, F.; Moll, M. Unexpectedly Facile Formation of Diazene Complexes and a New Type of Diastereomerism: [μ-N₂H₂{Fe(PPR₃)('S₄')}]₂ and Analogous Complexes with [FeS]-Centers. ('S₄'²⁻= 1,2-Bis(2-mercaptophenylthio)ethane(2-)). *Z. Naturforsch. B* **1994**, *49*, 76–88.
- (37) Sellmann, D.; Fürsattel, A.; Sutter, J. The Nitrogenase Catalyzed N₂ Dependent HD Formation: A Model Reaction and Its Significance for the FeMoco Function. *Coord. Chem. Rev.* **2000**, *200–202*, 545–561.
- (38) Sellmann, D.; Engl, K.; Heinemann, F. W.; Sieler, J. Coordination of CO, NO, N₂H₂, and Other Nitrogenase Relevant Small Molecules to Sulfur-Rich Ruthenium Complexes with the New Ligand 'tpS₄'²⁻= 1,2-Bis(2-Mercaptophenylthio)Phenylene(2-). *Eur. J. Inorg. Chem.* **2000**, *2000* (5), 1079–1089.
- (39) Sellmann, D.; Kaeppeler, J.; Moll, M.; Knoch, F. Transition Metal Complexes with Sulfur Ligands. 95. Diazene, Hydrazine, Ammine and Azido Complexes with Sulfur Dominated [Ru(PPh₃)('buS₄')] Fragments ('buS₄'²⁻= 1,2-Bis(2-Mercapto-3,5-Di-Tert-Butylphenylthio)Ethanato(2-)). *Inorg. Chem.* **1993**, *32*, 960–964.
- (40) Sellmann, D.; Gerlach, R.; Jödden, K. Reaktionen an Komplexgebundenen Liganden. XXXII.: Synthese Und Eigenschaften von Heteronuklearen Mangan-Chrom-Komplexen Mit Distickstoff-Diazene- Und Hydrazin-Brückenliganden. *J. Organomet. Chem.* **1979**, *178*, 433–447.
- (41) Cheng, T. Y.; Peters, J. C.; Hillhouse, G. L. Reactions of Coordinated Diazene in Ruthenium and Tungsten Complexes. Deprotonation of Ligated NH: NH and Subsequent Hydrogen-Migration to Carbonyl Ligands to Give Metal Formyls. *J. Am. Chem. Soc.* **1994**, *116*, 204–207.
- (42) Sellmann, D.; Jödden, K. [C₃H₅(CO)₂Mn-N₂H₂-Cr(CO)₅], a Complex with a Diazene Bridge and Two Different Coordination Centers. *Angew. Chem. Int. Ed.* **1977**, *16*, 464–465.

- (43) Sellmann, D.; Kleinschmidt, E. Synthesis and Properties of Rhenium Complexes with N₂, N₂H₂, N₂H₄ and NH₃ Ligands. *Z. Naturforsch. B* **1977**, *32*, 795–801.
- (44) Sellmann, D.; Brandl, A.; Endell, R. Cis-Diiminebis(Pentacarbonyl)tungsten. *Angew. Chem. Int. Ed.* **1973**, *12*, 1019–1020.
- (45) Field, L. D.; Li, H. L.; Dalgarno, S. J.; Turner, P. The First Side-on Bound Metal Complex of Diazene, HN=NH. *Chem. Commun.* **2008**, 1680–1682.
- (46) Li, Y.; Li, Y.; Wang, B.; Luo, Y.; Yang, D.; Tong, P.; Zhao, J.; Luo, L.; Zhou, Y.; Chen, S.; Cheng, F.; Qu, J. Ammonia Formation by a Thiolate-Bridged Diiron Amide Complex as a Nitrogenase Mimic. *Nat. Chem.* **2013**, *5*, 320–326.
- (47) Suzuki, S.; Toda, T.; Kuwata, S. A Diazene-Bridged Diruthenium Complex with Structural Restraint Defined by Single Meta-Diphosphinobenzene. *Dalt. Trans.* **2021**, doi: 10.1039/D0DT04398B.
- (48) Gu, N. X.; Oyala, P. H.; Peters, J. C. Hydrazine Formation via Coupling of a Nickel(III)–NH₂ Radical. *Angew. Chem. Int. Ed.* **2021**, *60*, 4009–4013.
- (49) Saouma, C. T.; Müller, P.; Peters, J. C. Characterization of Structurally Unusual Diiron N_xH_y Complexes. *J. Am. Chem. Soc.* **2009**, *131*, 10358–10359.
- (50) Sellmann, D.; Hille, A.; Rösler, A.; Heinemann, F. W.; Moll, M.; Brehm, G.; Schneider, S.; Reiher, M.; Hess, B. A.; Bauer, W. Binding N₂, N₂H₂, N₂H₄, and NH₃ to Transition-Metal Sulfur Sites: Modeling Potential Intermediates of Biological N₂ Fixation. *Chem. Eur. J.* **2004**, *10*, 819–830.
- (51) Sellmann, D.; Fürsattel, A. Modeling a Nitrogenase Key Reaction: The N₂-Dependent HD Formation by D₂/H⁺ Exchange. *Angew. Chemie Int. Ed.* **1999**, *38*, 2023–2026.
- (52) Sellmann, D.; Hennige, A.; Heinemann, F. W. Transition Metal Complexes with Sulfur Ligands Part CXXIX. Retention and Reactivity of the [Fe–NH=NH–Fe] Chromophore in the Iron Sulfur Diazene Complex [μ₂-N₂H₂{Fe(PPR₃)('S₄')}]₂ in Exchange and Oxidation Processes. ('S₄'²⁻ = 1,2-Bis (2-Mercaptophenylthio). *Inorganica Chim. Acta* **1998**, *280*, 39–49.
- (53) Collman, J. P.; Hutchison, J. E.; Lopez, M. A.; Guilard, R.; Reed, R. A. Toward a Dinitrogen Electroreduction Catalyst: Characterization of a Bis-Ammine, a μ₂-Hydrazine, a μ₂-Diazene, and a Remarkably Stable μ₂-Dinitrogen Complex of a Ruthenium Cofacial Diporphyrin. *J. Am. Chem. Soc.* **1991**, *113*, 2794–2796.
- (54) Köthe, C.; Braun, B.; Herwig, C.; Limberg, C. Synthesis, Characterization, and Interconversion of β-Diketiminato Nickel N_xH_y Complexes. *Eur. J. Inorg. Chem.* **2014**, *2014*, 5296–5303.
- (55) Shanahan, J. P.; Szymczak, N. K. Hydrogen Bonding to a Dinitrogen Complex at Room Temperature: Impacts on N₂ Activation. *J. Am. Chem. Soc.* **2019**, *141*, 8550–8556.
- (56) Geri, J. B.; Shanahan, J. P.; Szymczak, N. K. Testing the Push–Pull Hypothesis: Lewis Acid Augmented N₂ Activation at Iron. *J. Am. Chem. Soc.* **2017**, *139*, 5952–5956.
- (57) Simonneau, A.; Etienne, M. Enhanced Activation of Coordinated Dinitrogen with P-Block Lewis Acids. *Chem. Eur. J.* **2018**, *24*, 12458–12463.
- (58) Shanahan, J. P.; Szymczak, N. K. Lewis Acid Effects on Calculated Ligand Electronic Parameters. *Organometallics* **2020**, *39*, 4297–4306.
- (59) Sippel, D.; Rohde, M.; Netzer, J.; Trncik, C.; Gies, J.; Grunau, K.; Djurdjevic, I.; Decamps, L.; Andrade, S. L. A.; Einsle, O. A Bound Reaction Intermediate Sheds Light on the Mechanism of Nitrogenase. *Science* **2018**, *359*, 1484–1489.
- (60) (a) Kang, W.; Lee, C. C.; Jasniewski, A. J.; Ribbe, M. W.; Hu, Y. Structural Evidence for a Dynamic Metallocofactor during N₂ Reduction by Mo-Nitrogenase. *Science* **2020**, *368*, 1381–1385. (b) Peters, J. W.; Einsle, O.; Dean, D. R.; DeBeer, S.; Hoffman, B. M.; Holland, P. L.; Seefeldt, L. C. Comment on “Structural evidence for a dynamic metallocofactor during N₂ reduction by Mo-nitrogenase” *Science* **2021**, *371*, eabe5481. (c) Kang, W.; Lee, C. C.; Jasniewski, A. J.; Ribbe, M. W.; Hu, Y. Response to Comment on “Structural evidence for a dynamic metallocofactor during N₂ reduction by Mo-nitrogenase” *Science* **2021**, *371*, eabe5856.
- (61) Gardner, E. J.; Cobb, C. R.; Bertke, J. A.; Warren, T. H. Tris(Pyrazolyl)Borate Copper Hydroxide Complexes Featuring Tunable Intramolecular H-Bonding. *Inorg. Chem.* **2019**, *58*, 11248–11255.
- (62) Cox, J.D.; Wagman, D.D.; Mevedev, V. A. *CODATA Key Values for Thermodynamics*, 1st ed.; Hemisphere Publishing Corp: New York, 1984.
- (63) Chalkley, M. J.; Del Castillo, T. J.; Matson, B. D.; Roddy, J. P.; Peters, J. C. Catalytic N₂-to-NH₃ Conversion by Fe at Lower Driving Force: A Proposed Role for Metallocene-Mediated PCET. *ACS Cent. Sci.* **2017**, *3*, 217–223.
- (64) Kitajima, N.; Fujisawa, K.; Fujimoto, C.; Morooka, Y.; Hashimoto, S.; Kitagawa, T.; Toriumi, K.; Tatsumi, K.; Nakamura, A. A New Model for Dioxygen Binding in Hemocyanin. Synthesis, Characterization, and Molecular Structure of the μ-η²:η² Peroxo Dinuclear Copper(II) Complexes, [Cu(HB(3,5-R₂pz₃))]₂(O₂) (R = Isopropyl and Ph). *J. Am. Chem. Soc.* **1992**, *114*, 1277–1291.
- (65) The calculated τ₄ structural parameter judges the geometry of four-coordinate centers on a scale of 0 to 1, where 0 is perfectly square planar and 1 is perfectly tetrahedral. Our calculated τ₄ for respective Cu centers of **2c** (0.67) and **3** (0.75) indicate that they exhibit to varying degrees, distorted tetrahedral geometries. For further details regarding the τ₄ structural parameter please refer to: Rosiak, D.; Okuniewski, A.; Chojnacki, J. Novel Complexes Possessing Hg–(Cl, Br, I)–OC Halogen Bonding and Unusual Hg₂S₂(Br/I)₄ Kernel. The Usefulness of τ₄ Structural Parameter. *Polyhedron* **2018**, *146*, 35–41.
- (66) Sandström, J.; Sandström, J. S. *Dynamic NMR Spectroscopy*; Academic Press, 1982.
- (67) Back, R. A. The Preparation, Properties and Reactions of Diimide. *Rev. Chem. Intermed.* **1984**, *5*, 293–323.
- (68) The τ₅ structural parameter judges the geometry for five-coordinate centers on a scale of 0 to 1, where 0 is perfectly square pyramidal, and 1 is perfectly trigonal bipyramidal. The τ₅ calculated for the Cu center of **7** (0.50) indicates that it exhibits a highly distorted coordination geometry exactly between square pyramidal and trigonal bipyramidal. For further details regarding the τ₅ structural parameter please refer to: Addison, A. W.; Rao, T. N.; Reedijk, J.; van Rijn, J.; Verschoor, G. C. Synthesis, Structure, and Spectroscopic Properties of Copper(II) Compounds Containing Nitrogen–Sulphur Donor Ligands; the Crystal and Molecular Structure of Aqua[1,7-Bis(N-Methylbenzimidazol-2'-Yl)-2,6-Dithiaheptane]Copper(II) Perchlorate. *J. Chem. Soc. Dalt. Trans.* **1984**, 1349–1356.
- (69) Zhang, S.; Melzer, M. M.; Sen, S. N.; Çelebi-Ölçüm, N.; Warren, T. H. A Motif for Reversible Nitric Oxide Interactions in Metalloenzymes. *Nat. Chem.* **2016**, *8*, 663–669.
- (70) Dyadchenko, V. P.; Belov, N. M.; Dyadchenko, M. A.; Slovokhotov, Y. L.; Banaru, A. M.; Lemenovskii, D. A. A Complex of Gold(I) Benzenethiolate with Isocyanide: Synthesis and Crystal and Molecular Structures. *Russ. Chem. Bull.* **2010**, *59*, 539–543.
- (71) Craig, N. C.; Appiah, K. J.; Miller, C. E.; Seiden, M. V.; Varley, J. E. Reevaluation of Matrix-Isolation Infrared Spectra of the Isotopologues of Trans-Diazene and Attempts to Prepare Cis-Diazene by Photoisomerization. *J. Mol. Spectrosc.* **2015**, *310*, 3–7.
- (72) Mayer, J. M. Understanding Hydrogen Atom Transfer: From Bond Strengths to Marcus Theory. *Acc. Chem. Res.* **2011**, *44*, 36–46.
- (73) Zhang, S.; Fallah, H.; Gardner, E. J.; Kundu, S.; Bertke, J. A.; Cundari, T. R.; Warren, T. H. A Dinitrogen Dicopper(I) Complex via a Mixed-Valence Dicopper Hydride. *Angew. Chem. Int. Ed.* **2016**, *55*, 9927–9931.
- (74) Pappas, I.; Chirik, P. J. Catalytic Proton Coupled Electron Transfer from Metal Hydrides to Titanocene Amides, Hydrazides and Imides: Determination of Thermodynamic Parameters Relevant to Nitrogen Fixation. *J. Am. Chem. Soc.* **2016**, *138*, 13379–13389.
- (75) Keith, J. A.; Carter, E. A. Theoretical Insights into Pyridinium-Based Photoelectrocatalytic Reduction of CO₂. *J. Am. Chem. Soc.* **2012**, *134*, 7580–7583.
- (76) Tshepelevitsh, S.; Kütt, A.; Lökov, M.; Kaljurand, I.; Saame, J.; Heering, A.; Plieger, P. G.; Vianello, R.; Leitao, I. On the

Basicity of Organic Bases in Different Media. *European J. Org. Chem.* **2019**, *2019*, 6735–6748.

(77) Warren, J. J.; Tronic, T. A.; Mayer, J. M. Thermochemistry of Proton-Coupled Electron Transfer Reagents and Its Implications. *Chem. Rev.* **2010**, *110*, 6961–7001.

(78) Chalkley, M. J.; Oyala, P. H.; Peters, J. C. Cp* Noninnocence Leads to a Remarkably Weak C–H Bond via Metallocene Protonation. *J. Am. Chem. Soc.* **2019**, *141*, 4721–4729.

(79) Kani, N. C.; Prajapati, A.; Collins, B. A.; Goodpaster, J. D.; Singh, M. R. Competing Effects of PH, Cation Identity, H₂O Saturation, and N₂ Concentration on the Activity and Selectivity of Electrochemical Reduction of N₂ to NH₃ on Electrodeposited Cu at Ambient Conditions. *ACS Catal.* **2020**, *10*, 14592–14603.

Insert Table of Contents artwork here

